Optical Sensor for Measurement of Clad Height during Laser Cladding Process

by

Matthew Asselin

A thesis
presented to the University of Waterloo
in fulfillment of the
thesis requirement for the degree of
Master of Applied Science
in
Mechanical Engineering

Waterloo, Ontario, Canada 2006

AUTHOR'S DECLARATION FOR ELECTRONIC SUBMISSION OF A THESIS

I hereby declare that I am the sole author of this thesis. This is a true copy of the thesis, including any required final revisions, as accepted by my examiners.

I understand that my thesis may be made electronically available to the public.

Abstract

The process of laser cladding consists of depositing successive layers of molten metallic powder to create a near-net shape. A high-power laser is used to melt incoming metallic powder, which forms a melt pool on the surface. As the latter moves beneath the laser, this newly created melt pool solidifies. By properly controlling the trajectory of deposition tracks, one can create a diverse range of shapes with varying complexities. However, the process is very sensitive to parameters, requiring constant attention from technicians. This lends itself perfectly to the addition of automatic controllers whereby supervision is minimal.

In this thesis, an optical sensor is developed to monitor the process zone. The sensor will output a measurement of the height of solidified clad, which in turn can be used by a controller to adjust this geometrical feature. The thesis is divided into three main parts, each contributing to the final algorithm.

First, in Chapter 3 an analysis is performed on the light irradiating from the interaction zone (or melt pool). It is stated that the dominating source of light is governed by blackbody radiation from this molten metal. This is confirmed by analyzing a series of images captured through a digital camera, where various narrow bandpass filters were utilized to selectively view a portion of the CCD-sensor's spectrum. This investigation also leads to the selection of bandpass filter such that a stable, relatively intense melt pool is captured through the digital camera's CCD-sensor.

Second, in Chapter 4 the captured images are taken through a pair of image processing techniques, outputting a series of coordinates representating the melt pool's boundary. The image is first analyzed to calculate an optimal threshold level based on the minimization of fuzzy entropy. With this threshold selected, the grayscale image is converted into black-and-white, where the white pixels represent the melt pool. After this step, the melt pool's boundary is extracted through an 8-connectivity border tracing algorithm. This technique outputs a series of coordinates (in pixels) as though one were traveling along the melt pool in a clockwise rotation.

Last, Chapter 5 analyzes these pixel coordinates to extract the melt pool's height. The coordinates are first transformed into real-world coordinates, by use of a perspective transformation. This transformation essentially yields the melt pool's shadow, as created by a light-source coincident with the camera. As a result, the melt pool's

height is estimated based upon a right-angle triangle, where the camera's angle is known, and the projected coordinates represent the shadow length (triangle's base).

The result of applying this series of steps to the estimation of clad heights is found at the end of Chapter 5. Results varied dramatically, from 4% error to 393%. Although the errors are large at times, they are mainly caused by a bias in the estimate. That is, the dynamics of the true clad formation are very well predicted by the algorithm, however, shifting by a certain amount. This amount varies both with substrate velocity, and the clad's direction of travel, relative to the camera. A partial explanation is given such that the clad's height is offset from the laser center-point, which is a function of both these parameters. However, the specific relationship requires further experimentation.

Acknowledgments

I would like to take this opportunity to acknowledge many people for their help and support during this stage of my academic career. First, without the guidance and technical support of Amir Khajepour, Ehsan Toyserkani and Steve Corbin, this thesis would not be possible. Also, to my numerous colleagues that have given me enormous help and advice during development and testing periods, thank you very much. This includes: Jeff McIsaac, Mehrdad Iravani and Masoud Alimardani. To my three roommates, especially Rassin Grantab, and to my close friends in the area and elsewhere (Aleks, Brad, Dean, Justin, and Slavko), you have provided me with many unforgettable memories and friendships that will last a lifetime. Moreover, to the wonderful Chantal Duke: 'wink–wink'; you have been amazing. Last, and most importantly, I would like to thank my family, for whom this would not be possible. To my parents and siblings, your inspiration and support has been tremendous over the past years, and this is certainly proof.

Contents

List of Figures

ix

xi

List of Tables

Chapter 1

Introduction

In the past few decades, developments in laser systems, computer aided design (CAD), and additive manufacturing techniques [1] have given rise to a new trend in manufacturing: rapid-prototyping (RP). RP is a technique allowing designers to directly construct a part from a computer model. First, a model is designed in a CAD package where it is then sliced into many thin layers. The information of each layer is then passed to a rapid-prototyping machine, which utilizes the focused energy of lasers to build each successive layer.

In conventional techniques, a designer's part would be constructed from either a mold or die, or as a result of some machining steps. A mold or die requires special fabrication unique to each part, where experience and time are key. Machining also requires the attention of an experienced machinist, can require many different tools and steps before completion, and can produce limited geometries. Machining techniques are known as subtractive methods, whereby material is removed to fabricate a part. On the other hand, RP methods use additive manufacturing techniques. A blank substrate works as a base onto which material is deposited at precise locations to form a part, layer-by-layer.

Additive manufacturing provides many advantages over the traditional subtractive methods. According to Watkins [2], RP-tecniques have considerable savings in both cost and delivery time. In the early days of RP-technologies, Waterman states that production time can be cut up to 70%, while time-to-market reduced up to 90% [3]. In addition, due to the nature of the subtractive techniques, there is a larger amount of

wasted-material, as opposed to additive techniques which attempt to administer only what is required. Also, complexity of objects are limited with traditional techniques, whereby RP-methods can build upon these. For example, some RP-methods are capable of producing hollow shapes, where a traditional NC machining operation cannot. In addition, RP machines are highly automated, such that an operator can merely upload its CAD model and start the machine. This reduces the amount of supervision and expertise required.

RP-technologies have allowed designers to better refine their models by producing near-net shape prototypes with minimal effort and time. In the next section, a series of different RP-methods will be discussed, culminating with Laser Cladding. This technique of RP is the basis for the report, whereby a feedback sensor is developed to measure the final solidified height of a deposited clad.

1.1 Rapid-Prototyping and Laser Cladding

The process of Laser Cladding (LC) consists of adding successive layers to a substrate, producing a fully functional, near-net three-dimensional shape. The LC process is part of a larger group of rapid prototyping technologies, whereby material is added and not removed, to create a part. Other RP techniques include: stereolithography, selective laser sintering, laminated object manufacturing, and 3D printing (see [4, 5] for additional variations on these main techniques). These methods will now be described, along with associated advantages and disadvantages:

1. **Stereolithography (SL)**, first introduced in the late 1980s, is a technique by which a photo-sensitive monomer resin solidifies into a larger polymer molecule with exposure to an ultraviolet (UV) source [4]. This UV source is provided by a laser beam, which traces the desired path on the resin, thus solidifying it. A substrate is placed inside a pool of resin, where after tracing one layer with a laser-source, the substrate is lowered. This reveals uncured resin for which another layer can be traced. After all layers are traced, the part must be further cured by placing it under a fluorescent light, rendering it fully solid. Different types of materials can be used, however, are mainly from the family of acrylics

and epoxies [4]. The technique is well established in the industry, and provides tolerances comparable to NC machining, with reasonable producting times [4]. On the other hand, the limited materials are expensive and toxic, and must be constantly shielded from ambient light to prevent premature solidification [4]. Also, there is often a need for support structures for over-hanging sections, which must be accounted for in the design stage, and removed after production [1].

2. **Selective laser sintering (SLS)** was developed in the late 1980s, at the University of Texas Austin [6]. In SLS, a low-power laser is used to sinter powder particles, as opposed to liquid resin as with SL. The laser heats the powder particles to break surface tensions, allowing fusion between neighboring particles [4]. As explained by Klocke *et. al.* [7], the working material is preheated to a temperature just below that of melting, thus reducing the thermal gradient caused by laser interaction. After each layer, a fresh deposition of powder is applied to the part, and the procedure is repeated. This technique is capable of producing parts of many different materials, ranging from polymers, to metallic-based, to ceramics [5]. In general, these materials are less toxic than SL-materials, and can be processed with a low-powered laser (<100W) [4]. However, many of these materials require longer cooling-times, thus reducing the time-to-part production, and can be sensitive to heat and laser variables, thus parameters are specific to the material in question [4].

3. **Laminated object manufacturing (LOM)** is a technique by which successive layers of thin sheets are bonded together. First, a thin sheet of material is placed onto a substrate, whereby a laser cuts the desired pattern based on the sliced CAD model. The laser only penetrates through the thickness of the material. A hot roller then passes over the cut sheet, activating a bonding chemical [4]. Another sheet is then placed over this last one, whereby the second layer is cut with the laser. Again, a hot roller bonds the two layers together and the process is repeated. Excess material is cut into small squares, and remains on the structure to provide support for overhanging sections [4]. These small squares are more easily removed afterwards. This process lends itself to having quick

production times as only contours of each layer must be cut [4]. Also, many different materials can be used, such as polymer, metal or composite sheets [5]. On the other hand, there is a great deal of wasted material, which can also be difficult to remove [3], leading to limitations in hollow shapes. Moreover, the surface finish is relatively poor, and requires additional attention afterwards [4].

4. **3D printing** was developed at the Massachusetts Institute of Technology in the 1990s. The method consists of spreading a layer of powder over a substrate, after which a binder-chemical is deposited in a precise manner, solidifying the powder at this location [8, 5]. The binder is delivered through a printing-head, which is deposited according to the sliced version of a 3D CAD model. Additional powder is spread over the solidified material, where the process repeats, but for the next layer. Before the part can be fully solidified, it must be heat-treated to set this binder-chemical, followed by a final sintering step [4]. A major advantage to this technique is the lack of support structures required to produce over-hanging sections. However, powder can be trapped within cavities, thus the CAD model must contain holes or channels for the latter to escape [4].

In the past decade, the process of laser cladding has substantially grown in the market of rapid prototyping technologies. The LC process generally uses metallic powder, melted by a high-powered laser, and deposited onto a substrate. The molten metal solidifies as the laser-source moves through its predefined trajectory created from a sliced version of the original CAD model. Figure 1.1 illustrates the main components of a common LC system. As seen, a nozzle feeds powder to the laser, which in turn produces a pool of molten metal, known as the melt pool. As the subtrate moves, this melt pool solidifies to produce a metallic wall.

The system is rather simple, and builds on several disadvantages of the other techniques. For one, complex deposition paths can be created, including the tilt and rotation of the actual part itself. This allows hollow and overhanging sections to be produced without the worry of sagging or entrapped powder. Another advantage is that almost any type of material can be used, assuming it can be pulverized. This technique can also be expanded to produce heterogeneous components by simply adding multiple nozzles from different powder feeders. For example, one can begin
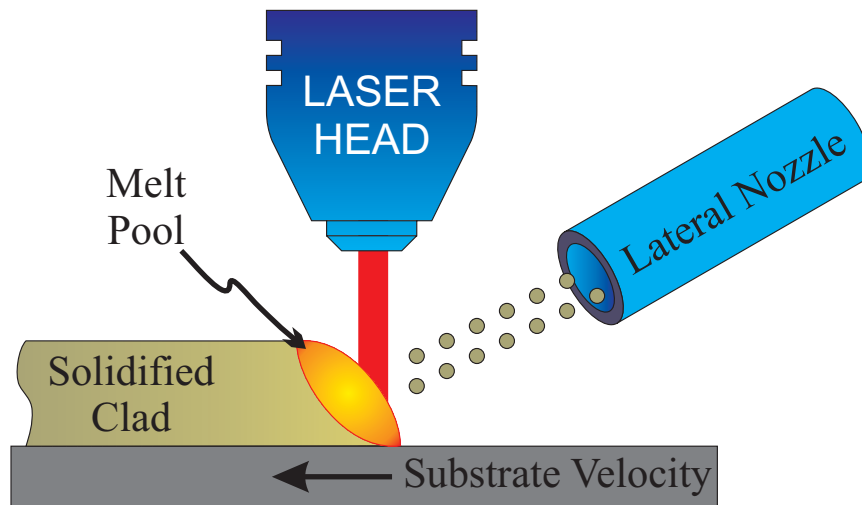
Figure 1.1: Main components involved in a laser cladding system.

with 100% stainless steel from powder feeder 1, and while building a thin wall, a second feeder can slowly begin to incorporate aluminum powder. This would create a wall of 100% stainless steel at the base, and slowly working its way to 100% aluminum at the top surface (or any other desired percentage combinations).

Many deviations to the setup of Figure 1.1 exist. For example, in this figure powder is injected through a lateral nozzle. This injects powder in one direction, usually with that of motion. However, powder can also be injected through a coaxial nozzle, which emits powder in a conical shape, with its focal point being the melt pool (Figure 1.2(a)). Another alternative is having the powder delivered in a direction vertical to the melt pool, while the laser source is at an angle to the latter (Figure 1.2(b)). In this technique, there are normally additional laser sources for symmetry. Another alternative to Figure 1.1 is to have the laser head move while the substrate is stationary, contrary to that shown in the figure. A combination of moving laser head and substrate is also possible, allowing for more complex geometries to be deposited. Last, some research groups [9] do not inject powder to the melt pool through a nozzle, but rather, pre-place powder onto the substrate (or previously deposited layer). As the laser passes over this pre-placed powder, the latter melts and bonds with the previous layer. This variation, however, approaches that of selective laser sintering.

(a) Coaxial nozzle delivering powder evenly to the melt pool, in a conical shape.

(b) Vertical nozzle to deliver powder to melt pool, with multiple laser sources at angles to the latter.
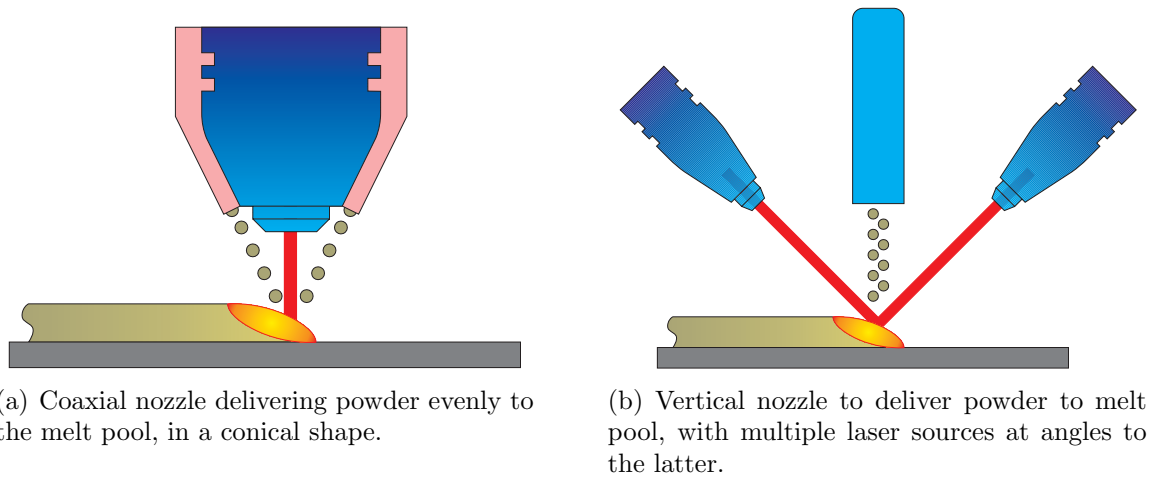
Figure 1.2: Two additional methods for delivering powder to the melt pool. Different techniques provide better qualities, such as surface finish and clad density.

Although the technique of laser cladding has many advantages, it is also prone to many of the common disadvantages of all rapid prototyping methods: sensitivity to both internal and external parameters. As will be further discussed in the report, the system is very sensitive to parameters that can, and cannot be directly controlled. For example, the final microstructure of a part is depicted by the cooling rate of the liquid metal. Therefore, controlling temperature gradients throughout the part is essential to having a desired microstructure.

1.2 Thesis Motivation, Objectives and Outline

As mentioned, laser cladding is very sensitive to variations in process parameters. Changes in these parameters lead to disturbances in the process, and in turn, the final product. It is therefore very important to monitor and control these properties. The majority of currently available LC machines utilize open-loop control strategies, whereby numerous experiments have provided empirical data on working ranges for various input parameters. In many situations, additional expert knowledge is required for online adjustments. This type of open-loop architecture lends itself to many limitations. For example, parameters must be optimized ahead of time for every possibly configuration of a part to be constructed, since the system cannot respond

during the process.

Many institutions are beginning to develop close-loop systems for better control of the process. The addition of close-loop control to a system of such sensitivity is imperative for competition in the market of RP technologies. In addition to increasing output quality, close-loop control will enable further automation, reducing the need for exhaustive experimentation and empirical studies, along with specialized technicians.

At the basis of all control systems lies the ability to measure properties of the process at hand. Laser cladding is no different, where several properties directly affect the final object. These properties, such as melt pool temperature, powder feedrates, substrate velocity, or focal distance of laser beam, have two main effects on the final part: metallurgical and geometrical. Metallurgical properties relate more to microscopic characteristics of the final object, such as its microstructure, porosity, and density. On the other hand, geometrical properties are seen to represent macroscopic details, such as dimensional tolerances and surface roughness. Both are very important, however, only geometrical features will be analyzed in this report. It should be noted that the clad's width and dilution into the previous layer are equally important to dimensional tolerances, however, will not be considered in this work.

One of the major criteria of RP technologies is producing accurate parts, with tolerances comparable to existing traditional techniques. Monitoring the dimensions of deposited material is therefore crucial to the sustainability of laser cladding in the rapid-prototyping industry. Since LC is a layer-by-layer deposition process, it is therefore very important to deposit consistent clads of specified height. This is where the addition of a close-loop controller will drastically help maintain accuracies, assuming a feedback sensor is capable of producing height measurements in real-time.

The objective of this report is to develop such a sensor, capable of monitoring the height of a deposited clad, in real-time. Due to the nature of the process, it is very difficult to physically attach a sensor to the workpiece for measurement. Therefore, a non-contact sensor is required, and with recent advances in CCD-technologies, the cost of CCD-cameras has become more than feasible, rendering them as perfect measurement devices for this application.

The remainder of this report will consist of the development and testing of a non-contact, CCD-based measurement device for monitoring clad height formation

in real-time. Chapter 2 will provide background information on advances in the laser cladding industry, along with feedback sensors pertinent to this report. Subsequently, Chapter 3 describes the lighting conditions relevant to capturing useful pictures during the process. The following two chapters will then deal with analysis of these pictures, where Chapter 4 describes melt pool segmentation from an image, and Chapter 5 is the analysis of this melt pool to determine the clad's solidified height. This chapter will also contain experimental verification of the algorithms. Overall conclusions and recommendations will be found in the last section, namely Chapter 6.

Chapter 2

Literature Review and Background

2.1 Laser Cladding

Over the past few decades, many institutions have advanced the field of laser cladding to its present state. As a result of being studied at various academic settings around the world, the term *laser cladding* is not unique as to describing the physical process. Table 2.1 lists the various research programs around the world, along with their associated term for the process. In addition, several projects have also been commercialized (also listed in Table 2.1) as to compete with existing RP-technologies, and to provide new services to the industry.

2.2 Feedback Sensors

In the previous section, various institutions involved in the advancement of the laser cladding process where outlined. Through the various research programs, many different sensors have been developed to measure important parameters affecting the fabricated part. The majority of the sensors can be categorized into four main groups: powder measurements, temperature recordings, laser parameters, and geometrical characteristics. In the following paragraphs, each group will be discussed in further detail, whereby specific sensors developed by various authors are outlined.

The first group relates to sensors relevant to the measurement of powder charac-

Institution, Commericalization	Country
National Research Centre, AccuFusion 　　—*Freeform Laser Consolidation (FLC)*	CANADA
University of Waterloo, SmartFabrication 　　—*Laser Cladding* 　　—*Laser Powder Deposition*	CANADA
University of Liverpool 　　—*Laser Cladding and Direct Fabrication* 　　—*Direct Laser Fabrication (DLF)*	ENGLAND
Electrolux Rapid Development 　　—*Direct Metal Laser Sintering (DMLS)*	FINLAND
Fraunhofer Institute for Production Technology 　　—*Controlled Metal Build-Up (CMB)*	GERMANY
Raja Ramanna Centre For Advanced Technology 　　—*Laser Rapid Manufacturing (LRM)*	INDIA
Los Alamos National Laboratory 　　—*Direct Light Fabrication*	USA
Penn State University, AeroMet 　　—*Laser Additive Manufacturing^{TM}(LAM)*	USA
Sandia National Laboratory, Optomec Design Company 　　—*Laser Engineering Net Shaping^{TM}(LENS)* 　　—*Direct Metal Deposition Systems^{TM}(DMDS)*	USA
University of Michigan, Precision Optical Manufacturing 　　—*Direct Metal Deposition^{TM}(DMD)*	USA

Table 2.1: List of popular institutions with research interests in laser cladding. Synonymous names of the process are also listed, along with spin-off companies from associated affiliations.

teristics. This group is important as incoming powder is melted by a laser source, and will eventually solidify to form the final part. Properties, such as particle velocity, powder distribution from nozzle output, and carrier gas fluctuations can greatly affect the amount of powder captured in the melt pool, with end results directly applicable to the part. In 1996, Meriaudeau *et. al.* [10, 11] utilized one CCD-camera to measure powder stream distributions. At startup, the camera is capable of measuring the velocity of particles [1], allowing the operator to adjust carrier gas rates. During continuous operation, the sensor provides information regarding the shroud gas, used to shape the stream. This is obtained by measuring the width of the powder stream before contact with the melt pool. A year later, Meriaudeau *et. al.* [12] develop a second sensor for measurement of mass flow rates of incoming powder. The sensor consists of a light source (laser) shining through the powder stream (upstream of the nozzle), where a photo-voltaic cell records the amount of transmitted light. This provides information regarding dynamic changes from the mean powder flow rate. In 2003, Doubenskaia *et. al.* [13] publish their apparatus for measuring several parameters related to incoming powder: particle velocities and sizes, and temperature. As mentioned, their system is based on the work of Ignatiev *et. al.* [14] for thermal spraying, and consists of a regular CCD-camera with a bandpass filter in the near-infrared spectrum of 800-960nm. Since Doubenskaia is working with multiple powders, measuring the size and temperature of different powders within the stream allows online correction of powder distributions.

In the second category of feedback sensors, namely process temperature, there has been a significant amount of work. In 1990, Li and Steen [15] published work on utilizing a photo-diode to indirectly record melt-pool temperatures (in the 400-1250nm wavelength spectrum). Light irradiation from the melt pool was recorded, where process conditions were changed to reveal deviations in their mean voltage levels. This is partially the problem with photo-diodes: no spatial distribution. The sensor outputs a voltage proportional to the total light irradiated, and can therefore not distinguish where the latter is coming from. In 1996, Meriaudeau *et. al.* [10, 11] utilize radiation thermometry, a non-contact method for measuring surface temperatures. They use one camera, with a bandpass filter centered at 850nm (to steer clear of laser

---

[1]Velocity is measured through tracking of particle displacement in multiple image frames.

and atmospheric interference), to interpolate spatial surface temperature from pixels' gray-scale values. They obtained a resolution of 5^oC, with an accuracy of 15^oC up to a temperature of 800^oC. Although this range is not sufficiently high for melting typical steels, the use of a camera allows for spacial temperature distributions to be measured. In 1998, Fox *et. al.* [16] analyze the light irradiated back through the laser's optics for measuring melt pool temperatures. Light returning through the focus optics of the laser head is redirected to a chamber through means of ZnSe plate (transmits 99.8% of laser light). In the chamber, two wavelengths are selected ($650nm$ and $950nm$), whereby their intensities are compared to deduce the temperature using two-color pyrometry. In 2004, Doubenskaia *et. al.* [13] used a multi-wavelength 1-spot pyrometer and a two-dimensional pyrometer to measure surface temperatures during cladding operations. The pyrometers were composed of several photo-diodes, enabling spatial measurements. Both pyromaters were fully capable of measuring temperatures above the melting point of typical steels ($\sim1800K$). Results were given as temperature measurement deviations based on different cladding conditions. No information regarding true temperatures and measured temperatures were given.

The third category of feedback sensors relates to the energy supplied to the process zone. The amount of energy, and delivery methods are very important, as they dictate the amount and method of melting incoming powder. Depending on the type of laser (continuous or pulsed), different parameters can be monitored directly from the laser source's instruments, such as mean power, energy per pulse, or pulse duration. An interesting use of reflected radiation is done by Fox *et. al.* [16], which uses the information to keep the laser's focal point at a constant distance from the substrate (indirectly used to control the height). Their work is based on that of Haran *et. al.* [17], a year before them. Haran *et. al.* capture light reflected back through the optical system, and segment two wavelengths. A comparison is made between the two wavelength's focal distance on the receiving optics, which relate back to the original laser's focal distance with respect to the optics. Based on empirical data, they are capable of measuring the laser's offset distance.

Geometry-based sensors is the last main category where authors have concentrated their research. In 1996, Meriaudeau *et. al.* [10, 11] publish work relating to the measurement of melt pool shape. There is no information regarding the actual image

processing algorithms, merely empirical relationships between process parameters and the resultant height and width measurements. In 1997, another paper is presented by Meriaudeau *et. al.* [12] whereby the CCD-camera's placement is shown to face the direction of motion of the deposited clad. This allows them to gather information relating to clad height and width, along with the its cross-sectional profile. In 1999, Mazumder *et. al.* [18] publish their work relating to photo-diodes used in height measurement. The work presents results of using more than one sensor, however, no specific details on their algorithms for height extraction, due to the patented technology. Much of the work on geometrical sensors has concentrated on deviations from a predetermined measurement. For example, Fox *et. al.* [16] develop a control algorithm to keep the height at a constant level, which is accomplished based on the work of Haran *et. al.* [17], as mentioned in the previous paragraph. A recording is taken of the sensor's output for a given height, and the control scheme attempts to control the inputs to keep this measurement value. This appears to also be the result of Mazumder's work, where by the photo-diodes output a voltage, and when this voltage is exceeded, certain process parameters are changed to bring the voltage back down.

As seen, many sensors have been developed to measure various properties of the laser cladding process. This report is concentrated on the measurement of clad height during deposition, using one or more CCD-cameras. As seen from the various literature surveys, many uses of CCD-cameras have been accompanied by selection of proper bandpass filters, due to the high levels of light irradiation from the process, in addition to avoiding the laser's wavelength. Aside from this information, there are very little details as to image processing algorithms or their frequencies and camera placement or limitations on clad deposition directions. Also, there has been little to none comparison of true height and estimated height from the various algorithms. This may be attributed to many authors using their height sensor directly in a control scheme, whereby visual comparisons with, and without the latter on a part's final geometry.

Based on this lack of information in the literature, this thesis will concentrate on developing a sensor to measure the height of deposited clads in real-time. A discussion will be presented on the nature of the light irradiation from the process

zone, along with the selected bandpass filters. Also, a thorough presentation of the image processing algorithm is included, where limitations on clad's direction with respect to camera's position is established, along with the overall accuracy of the algorithm, with respect to true clad measurements taken offline.

Chapter 3

Camera Filter Selection

3.1   Introduction

The laser cladding process produces very intense light as a result of melting metallic powder by use of a high-power laser. Capturing frames of the process reveals purely white images, caused by saturation of the CCD-sensor from this intense irradiation. To properly view images of the melt pool region, the source and nature of this intense light must be defined. This will enable one to properly select filters for the cameras, allowing only a portion of the irradiation to be seen. It is desired to have this portion of light be representative of the melt pool zone.

In the following sections, a theoretical development will produce a hypothesis as to the nature of this irradiation. This will be followed by experimental results to confirm such claims, along with proper selection of optical hardware (*i.e.* filters).

Before continuing, a quick mention is made of a threshold algorithm used in this Chapter, however, only developed later in Chapter 4. The threshold algorithm is based upon minimizing the fuzzy entropy of an image. That is, in an 8-bit grayscale image, each pixel has a value between 1 and 256. Thresholding is the process by which each pixel is assigned to the foreground (value of 1) or background (value of 0). In this algorithm, a threshold is selected where all pixels below are assigned a value of 0, while all pixel values above are set to 1. A resultant measure of the image's entropy is given by a specific metric, and the threshold value yielding the minimal level is selected as the optimal threshold. In general, threshold levels obtained in this

manner are very good at segmenting the melt pool from the background objects. For this reason, the algorithm will used throughout this Chapter as a measure of light intensity, whereby large thresholds indicate a larger amount of light in the image than lower thresholds.

3.2   Theoretical Analysis

In many laser applications, such as laser welding, cutting, drilling, etc., the energy supplied to the material is sufficiently large to cause ionization of the elements. However, in the laser cladding process, the main purpose is to deposit molten metal on a substrate, building successive layers in a similar manner. The energy supplied is merely enough to melt the powder, and thus, the elements do not become overexcited, causing ionization (plasma). For this reason, the majority of light emitted from the process zone is caused by blackbody radiation of the molten powder due to its elevated temperature.

Typical temperatures encountered during the process are dependent upon the material being deposited. As previously mentioned, only a sufficient amount of energy required to melt the incoming powder is necessary, and thus, depending upon the type of powder, the melting temperature will vary. For stainless and tool steels, the dominant element is iron, which melts at $1811K$. However, from experimental testing temperatures can rise up to 2300-2400K [19]. This is especially true for the first layer deposited onto a substrate, where the energy supplied is not only for melting the incoming powder, but is also utilized to melt the substrate, creating good bonding of the two.

Max Planck developed an equation describing blackbody radiation as a function of both temperature and wavelength [20], as seen below:

$$E(\lambda, T) = \frac{2\pi h c^2}{\lambda^5 \left(e^{hc/\lambda kT} - 1\right)} \tag{3.1}$$

where λ $[m]$ is the wavelength, $T[K]$ is the temperature, $h = 6.626 \times 10^{-34}[Js]$ is Planck's constant, $c = 3.00 \times 10^8[ms^{-1}]$ is the speed of light, and $k = 1.381 \times 10^{-23}[JK^{-1}]$ is Boltzmann's constant. It is seen that radiation emitted varies not
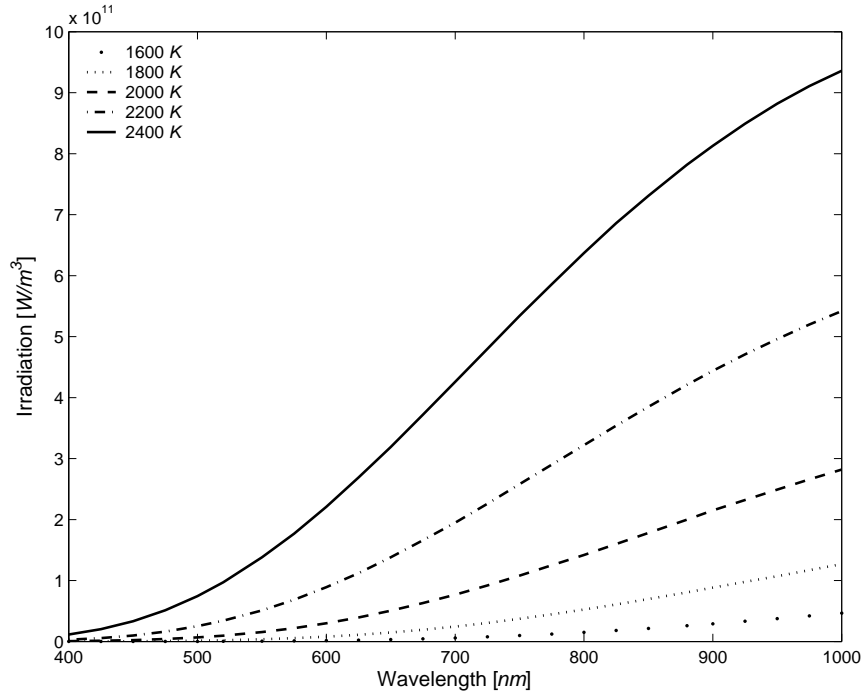
Figure 3.1: Hypothetical irradiation from melt pool zone, as characterized by Max Plank's blackbody radiation. Temperatures reflect typical laser cladding operating conditions. Wavelength range selected according to CCD-sensor's range (UNIQ 600CL Digital Camera).

only with the temperature of the body, but is also non-uniform throughout the electromagnetic spectrum. For this reason, it is important to analyze Planck's equation in the spectrum visible by the CCD-sensor, which extends from $400nm$ to $1000nm$ [1]. A graphical representation of Equation (3.1) is seen in Figure 3.1 for the aforementioned spectrum. Several curves are plotted for various temperatures, representing typical values encountered during the process. As can be seen, the amount of irradiation increases with both wavelength and temperature. Thus, in the captured image, since the melt pool has the greatest temperature, it should appear with brightest pixel values. This should be of great help when segmenting the melt pool from the background information of the image, as long as saturation of the CCD-sensor does not impede the algorithm, as will be discussed later.

The CCD-sensor used to capture this blackbody radiation during experiments does

---

[1]This information is provided by the camera manufacturer, for a UNIQ 600CL digital camera.

17
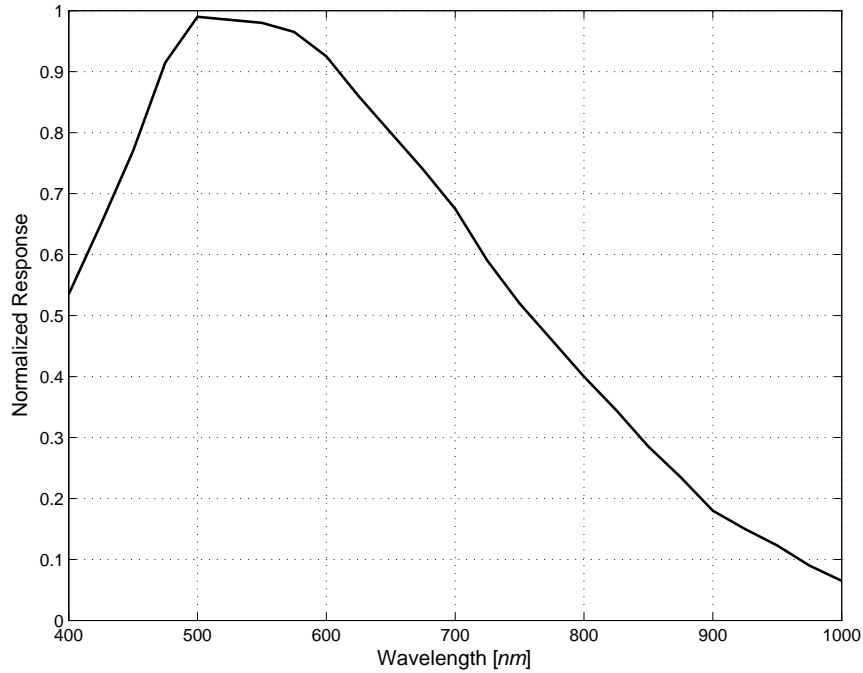
Figure 3.2: Response of CCD-sensor to incoming light. Bandpass-type response, with peak at $\sim 500nm$. (UNIQ 600CL Digital Camera)

not have a uniform gain throughout its spectrum. Figure 3.2 illustrates the spectral response of the sensor to incoming light. For example, according to this graph, light intensity of rays at $700nm$ would be attenuated by approximately 68%. As can be seen, it has almost unity gain in the range of $500nm$ to $550nm$. Outside of this range, the camera's response decreases in a relatively linearly manner. This non-uniform response is very important, as it will modify the incoming blackbody radiation from the process zone.

To evaluate the response of the CCD-sensor to the incoming light, the latter is attenuated in the spectrum by the former. That is, at every frequency channel, the theoretical blackbody radiation is multiplied by the CCD-sensor's attenuation, at this frequency. The result of this procedure is shown in Figure 3.3. These curves represent the light irradiated from the interaction zone, as seen by the digital cameras. From the spectral response of the sensor (Figure 3.2), the incoming signal (or light) is attenuated as the wavelength increases. However, the incoming blackbody radiation is the total opposite, as seen in Figure 3.1. The combined effect is seen in Figure

18
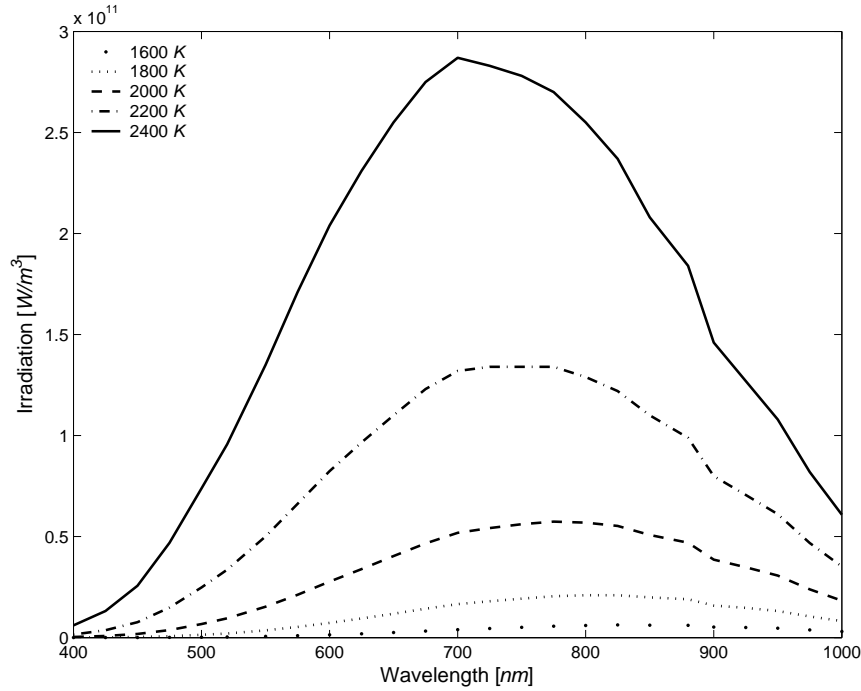
Figure 3.3: Actual light intensity, as seen by digital camera. This is obtained by multiplying the incoming blackbody radiation by the CCD-sensor's response, at each frequency channel. Again, temperatures representative of typical operating conditions in laser cladding.

3.3 where the attenuation dominates and the signal is decreased as the wavelength increases. The peak in curves of Figure 3.3 appears in the middle of the spectrum, where the CCD-sensor's attenuation was overshadowed by the amount of incoming light, thus producing peaks at approximately $700nm$. Before this peak, the incoming irradiation is very small (as seen by the theoretical curves), and coupled with the low gain from the CCD-sensor, produces even less light intensity in the lower wavelengths.

As previously mentioned, in order to reduce the effects of sensor saturation, a bandpass filter will be added to the camera's optical hardware which will allow irradiation from a specific wavelength to penetrate. In the next section, experimental verification will be provided for the theory developed in this section, followed by the selection of a proper bandpass filter.
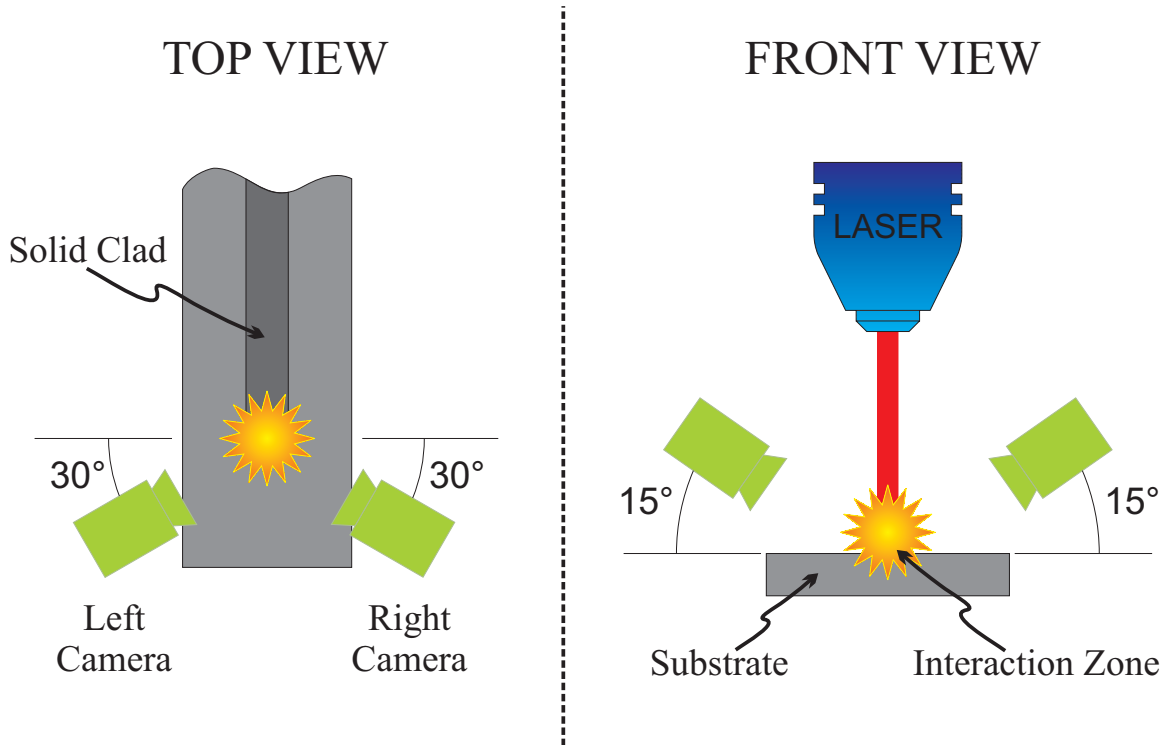
Figure 3.4: Experimental setup of cameras with respect to process zone. Cameras are symmetrical about this region and, have different bandpass filters in their optical hardware, based upon the experiment number (see Table 3.1).

3.3 Experimental Setup

In the previous section, the following hypothesis was introduced: blackbody radiation is the main source of light irradiating from the process zone, which is attenuated in a non-linear manner by the CCD-sensor, as shown in Figure 3.3. To evaluate this statement, a series of experiments are conducted such that the light intensity emitted and captured by the digital cameras are analyzed quantitatively.

For such experiments, two digital cameras (UNIQ UP-600CL) are setup in symmetrical locations about the process zone, each with a different bandpass filter added to its optical hardware, as seen in Figure 3.4.

Three bandpass filters are selected for the experimentation (manufactured by Edmund Optics). The filters have their center wavelengths at 520, 700 and $880\,nm$, and each has a width of $\pm 40\,nm$ (half-maximum full-width, $HMFW$, of $80\,nm$). As can be
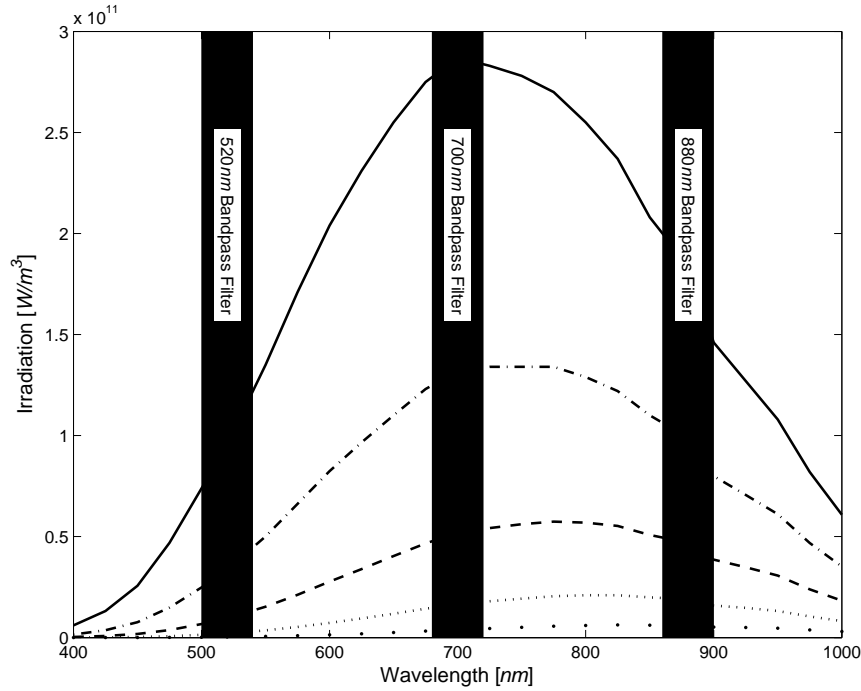
Figure 3.5: Location of bandpass filters with respect to light intensity, as registered by the CCD-sensors.

seen from Figure 3.5, where the filters are overlapped with the theoretical blackbody radiation as observed from the digital cameras, each filter should allow a different amount of light intensity to be observed by the CCD sensor. The maximum amount of light should be observed with the second filter, centered at $700\,nm$, while the filter centered at $520\,nm$ should yield the least amount of light.

To measure the amount of light seen by the CCD-sensor, images captured by the digital cameras are analyzed offline by means of calculating the optimal threshold value in order to segment the melt pool from the image. This optimal threshold value is found by means of a fuzzy threshold algorithm, which selects a threshold value based upon minimizing the image's entropy, as will be discussed in Chapter 4. As a simplistic view, the thresholding algorithm returns the average gray-level intensity of the melt pool, as a percentage of the maximum level. For example, if the fuzzy threshold is computed for two images, and the first returns an optimal threshold of 75%, while the second returns 60%, it indicates that there are a greater number of

Table 3.1: Bandpass filters used for each experiment, along with their location (right/left camera). Each filter is used twice: once per digital camera. This is to reduce any possible bias associated to a particular viewpoint or camera.

Experiment	Left Camera	Right Camera
1	$520nm$	$700nm$
2	$700nm$	$880nm$
3	$880nm$	$520nm$

bright pixels in the first image than in the second. This indicates that more light is being transmitted to the CCD-sensor in the first image, than in the second. Note that, the digital cameras utilized provide a maximum gray level of 255 (8 bit camera). Thus, for example, a threshold value of 60% represents a gray level of 153.

Since two digital cameras are available, and three filters are selected for evaluation, it is necessary to perform a minimum of two experiments: one experiment with the 520 and $700nm$ filters, the second with the 700 and $880nm$ filters (or 520 and $880nm$). This will produce a pair of results for one of the filters, while only a single set for the other two. Thus, an extra experiment is conducted, where the other two filters were used, thus yielding a pair of results for each filter. Also, the extra information is useful for providing information regarding repeatability and hardware-specific details, seeing as each filter is tested on a different camera. The combinations of filters for each experiment are listed in Table 3.1.

3.4   Results and Discussion

The results of applying the fuzzy thresholding algorithm to the set of images captured during the three experiments of Table 3.1 are found in Figure 3.6. The figure is divided into three columns, each having a series of 50 thresholded-images, which corresponds to the results of each experiment outlined in Table 3.1. The filter centered at $700nm$ consistently produces the greatest threshold level, indicating that the series of images captured with this filter had the greatest light intensity. On the other hand, the filter centered at $520nm$ consistently has the lowest threshold levels, indicative of the images having the least amount of light intensity. Again, the filter centered at
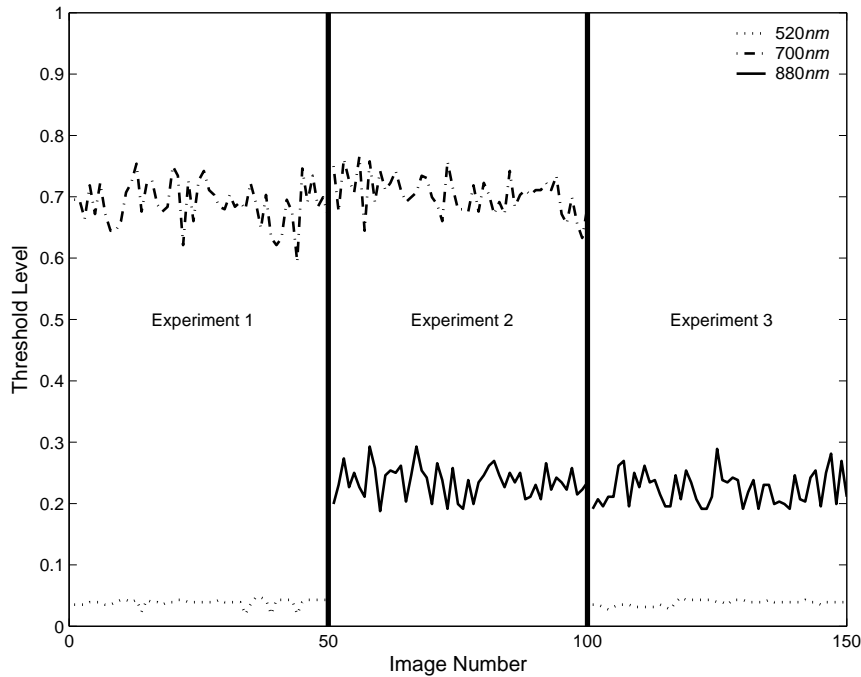
Figure 3.6: Optimal thresholds for each filter, computed over 50 images. Two cameras are used per experiment, thereby allowing only two filters to be tested per experiment. See Table 3.1 for details.

$880nm$ has consistently lower threshold values than the filter at $700nm$, while greater than that centered at $520nm$. These trends were fully predicted by the theoretical developments in the previous section.

To further visualize the threshold levels obtained throughout the three experiments, their average values are computed for each experiment, and are outlined in Table 3.2. In addition, the average value for each filter is computed, and plotted against the theoretical blackbody irradiation as seen from the CCD-sensor (see Figure 3.3) in Figure 3.7. As can be seen, tracing a best-fit curve through these later three points demonstrates the proper trend that the threshold levels follow. That is, it is expected to have the lowest light intensity from the filter centered at $520nm$, which corresponds to an average threshold level of 3.85%. As the wavelength increases, the theoretical blackbody irradiation as captured by the CCD-sensor equally increases (for increasing temperatures). With a filter centered at $700nm$, we have the largest average threshold value of the three filters tested, corresponding to 69.70%. From

Table 3.2: Average of 50 thresholds obtained for each bandpass filter, at every experiment. Overall average for each filter listed in last row of table.

Experiment	520nm	700nm	880nm
1	3.90%	69.00%	–
2	–	70.40%	23.60%
3	3.80%	–	22.40%
Average	3.85%	69.70%	23.00%

theoretical developments, in the temperature range of normal laser cladding conditions, it was noticed that the maximum irradiation is seen at approximately $700nm$, as verified experimentally by the average threshold values from the bandpass filters. After this filter, the average threshold value falls to 23.00% for a bandpass filter centered at $880nm$. This value is larger than the average threshold level at $520nm$, as expected. It was seen in Figure 3.3 that the light intensity seen by the CCD-sensor was greater at $880nm$ than at $520nm$, for the same temperature curve, as verified by this last result.

As previously mentioned, a bandpass filter is to be added to the digital camera's optical hardware. Without this filter, the amount of light irradiating from the process zone is too large for the CDD-sensor, and causes saturation of the pixels (*i.e.* image is all white). To select the proper filter, the threshold levels obtained from the previous three experiments were analyzed, along with the actual images obtained from the digital cameras. Figure 3.8 illustrates the entire section of thresholds calculated for experiments #1 and #2 of Table 3.1. As can be seen, the thresholds obtained for filters centered at $520nm$ and $880nm$ fluctuate throughout the experiments, as opposed to those obtained with a filter centered at $700nm$. The observed fluctuations are caused by changes in the process zone, such as melting of the incoming powder stream, or flares toward the incoming laser (caused by an insufficient powder stream, and thus melting of the substrate, or previous layer). These abnormal process conditions cause a larger amount of light to be irradiated. However, the digital cameras used throughout the experiments appear to greatly amplify the latter, due to unknown reasons. No matter the source of this additional light, the fluctuation of threshold levels is unwanted in the image processing algorithm.

Figure 3.9 illustrates a sample image captured using each of the three aforemen-
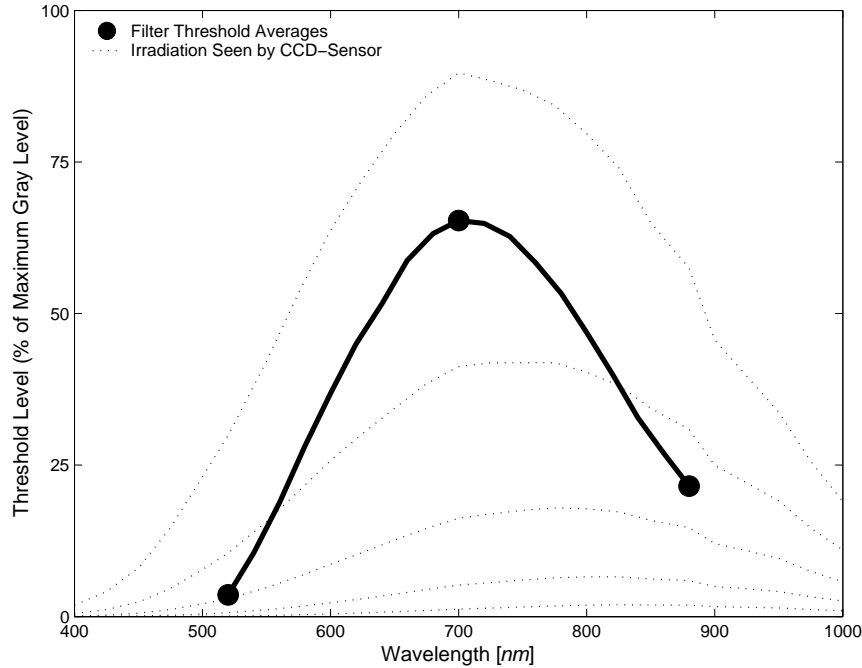
Figure 3.7: Average threshold level obtained for every bandpass filter, throughout all experiments. These results are overlayed with the hypothetical light intensity, as seen by the CCD-sensors. See Figure 3.3 for further details.

tioned filters in the optical hardware of the digital cameras. As can be seen, and as illustrated by the low threshold values, the melt pool is attenuated for the 520 and $880nm$ filters. With a bandpass filter at $700nm$, the melt pool is well seen by the digital camera, and there is large contrast between the foreground (melt pool) and the background objects. This contrast will be very important when attempting to segment the true melt pool from the image.

Based upon the results of Figures 3.8 and 3.9, the bandpass filter centered at $700nm$ is selected as the final filter for the digital camera's optical hardware. The threshold values obtained with this filter have little to no fluctuations during all process conditions, while the contrast between the melt pool and background objects is the most promising of the three.
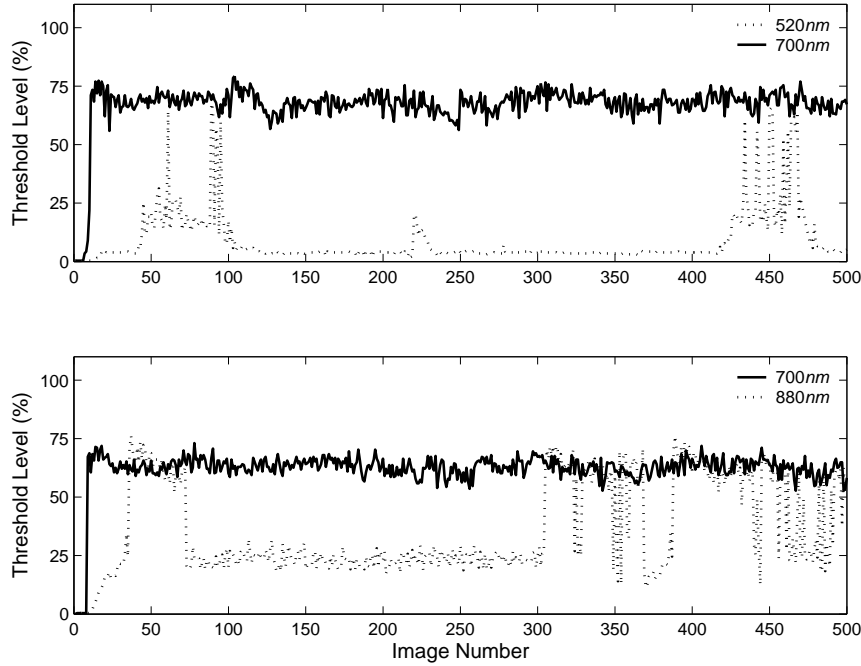
Figure 3.8: Threshold values obtained throughout entire experiments. Top and bottom figures correspond to experiments 1 and 2, respectively. Large spikes for filters at 520 and 880nm are caused by irregular process conditions, causing extra light to be emitted from the process zone. The 700nm filter appears to be unaffected by this additional light.

3.5   Conclusions

In Section 3.2, a theoretical analysis of the system's light irradiation was developed, stating that the process zone of the laser cladding system emitted purely blackbody radiation. It was stated that the temperatures encountered were not sufficient to cause any ionization of the material, and thus, the only source of light, aside from outside environmental sources, was caused by the elevated temperatures of the molten metal (1600-2400K for iron-based materials). In addition, the blackbody radiation emitted was not only a function of the body's temperature, but equally of the wavelength at which it was radiating. This was described by Planck's Law in Equation (3.1).

On the other end, incoming light is attenuated by the CCD-sensor in a non-linear manner, as shown in Figure 3.2. Applying this attenuation to the incoming light of Figure 3.1 produced the actual light, as seen by the CCD-sensor, resulting from the blackbody emission of the process zone (plotted in Figure 3.3). The camera's non-
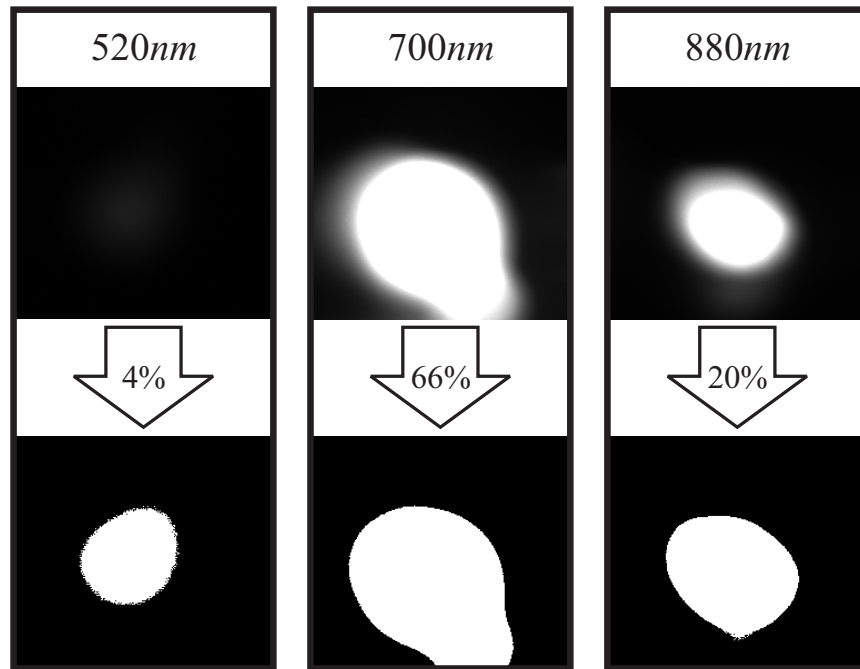
Figure 3.9: Sample image captured with each bandpass filter, along with the associated fuzzy-algorithm thresholds, segmenting the melt pool from the background.

uniform attenuation modified the incoming radiation such that, in the CCD-sensor's wavelength spectrum ($400nm$ to $1000nm$) and for the range of temperatures encountered ($1600K$ to $2400K$), the maximum irradiation was centered at approximately $700nm$.

These hypotheses were verified experimentally by calculating the optimal threshold level obtained from images where three bandpass filters were added to the digital camera's optical hardware (centered at $520nm$, $700nm$, and $880nm$). Three experiments were conducted, where two filters were used on two separate cameras during the cladding. The results were plotted in Figure 3.7, which show that the amount of light seen by the digital cameras is governed by blackbody radiation being attenuated by the CCD-sensor's non-uniform spectral distribution.

A bandpass filter centered at $700nm$ was then selected out of the three filters. This filter was shown to provide consistent, robust threshold measurements during varying process conditions, in addition to having the best contrast between melt pool and background objects, in the captured images.

Chapter 4

Image Analysis: Melt Pool Segmentation

4.1 Introduction

After the camera captures a frame from the process zone, the resulting image must undergo a series of image processing steps before the final measurements can be extracted. The first, and one of the most important steps, is to properly segment the melt pool from the grayscale image. This is accomplished by two steps: thresholding and boundary tracing. Thresholding is the process by which a grayscale image is transformed into a binary image. From this information, the boundary of the melt pool can be traced, resulting in a series of coordinates (in pixels) of the melt pool perimeter. These coordinates can then be transformed into real-world coordinates (such as millimeters or inches), and through an analytical solution, the desired measurements can be extracted.

In this chapter, the thresholding and boundary tracing operations will be discussed. First, thresholding of the grayscale image will be investigated, where two techniques will be evaluated to determine the optimal method. This will then be followed by the melt pool boundary tracing algorithm.

4.2   Image Thresholding

Image thresholding consists of associating each pixel from its grayscale value (or any other format, such as RGB, YUV, etc.) to either a background pixel (black pixel, value of 0) or a foreground pixel (white pixel, value of 1) [21]. The foreground pixels are normally associated with the desired objects for future analysis, while the background represents objects one wishes to ignore. This association is accomplished by selecting a threshold value within the grayscale range, where pixels above this level are associated to the foreground, and pixels below to the background (or vice-versa).

A static threshold value is normally used for pixels within the same image. In certain circumstances however, the threshold value can change spatially within the image, to allocate for different lighting conditions. From image to image, a static threshold value is also often used, reducing the amount of calculations to be performed, thus increasing the speed of the algorithm. However, adaptive threshold values may be used, where a new level is calculated based upon the new image. This requires an extra step in the processing, thus reducing the frequency at which images may be analyzed. This technique however, does allow for different lighting conditions to be assessed in a dynamic manner.

In the laser cladding process, the threshold level is kept static throughout the image, however, is adapted from frame-to-frame. This will allow for changes in the process to be accounted for, such as the addition of light to the image from powder-jet ignition, or large emission of light resulting from plasma phenomena.

Many techniques exist for the calculation of this threshold value. Sezgin and Sankur [21] associate thresholding techniques into six categories, based upon the information they exploit:

1. Histogram shape-based methods

2. Clustering-based techniques

3. Entropy-based algorithms

4. Object attribute-based techniques

5. Spatial distribution methods

6. Local methods (dynamic thresholding within the image)

The first method is based upon the shape of the histogram[1], exploiting the peaks and valleys of the image's histogram, or even the curvature and smoothness of the later. The second technique utilizes a clustering analysis of the gray-level data where the number of clusters is two. The third technique is based upon calculating the resulting entropy of the foreground and background pixels after thresholding. A criterion is used, such as maximization of image entropy, to select the optimal threshold. The fourth technique involves searching for a similarity between the original gray-scale image, and the binarized image, using criteria such as edge coincidence or fuzzy shape-similarity. The fifth algorithm, spatial distribution-methods, looks not only at pixel gray-levels, but also includes information regarding its neighbourhood of pixels. Last, the sixth technique calculates a new threshold at each pixel within the image, based upon statistical information at each location.

A typical melt pool image is shown in Figure 4.1. As can be seen, the image is rather simple, where the melt pool is easily distinguished from the background by an observer. The difficulty is with respect to fuzzy-borders, and possible reflections from the substrate or flaring in the process, as outlined in the image. Since the image is not dominated by background objects (background is essentially black), the aforementioned list of six thresholding techniques can be reduced down to two. The fourth, fifth and sixth techniques are more useful for images having multiple objects, or varying light intensities throughout the image, which is not the case for the process zone images. The first option, histogram shape-based, is often used when multiple peaks in the histogram occur, for various objects within the image, which again, is not the case. This leaves options two and three, corresponding to a more statistical-based approach with a clustering analysis and, maximization of information transfer with an entropy-based approach [21].

In the following section, a technique from these last two categories will be investigated, and followed by experimental verification. First, a statistical approach developed by Otsu [22] will be discussed, followed by a fuzzy-entropy algorithm by Huang and Wang [23].

---

[1]A histogram is a function that returns the number of pixels in one image for each graylevel. The sum of all pixels at all gray-levels is equivalent to the number of pixels in the total image.
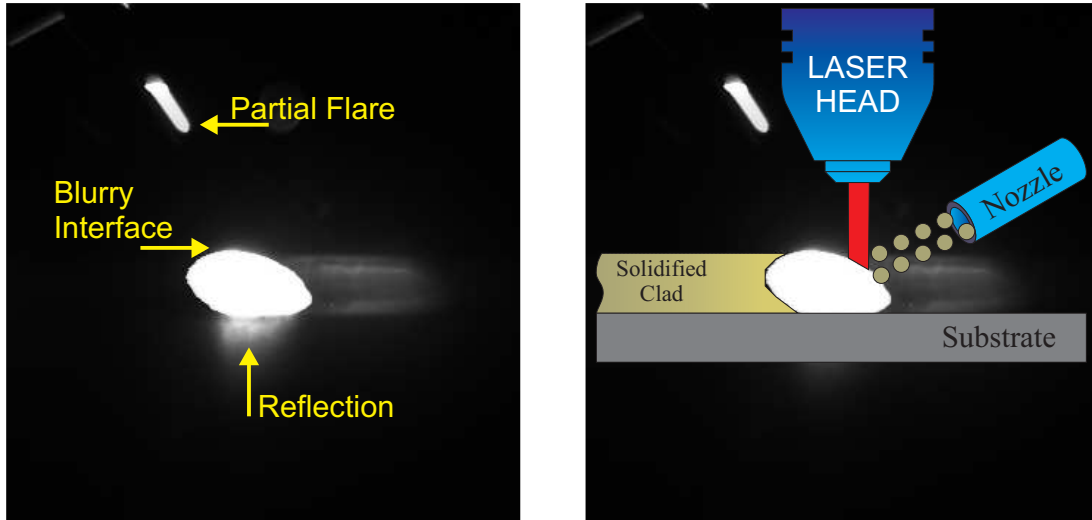
(a) Raw image from digital camera, with problematic features labeled.

(b) Annotated image with main components in process zone.

Figure 4.1: Typical image taken from digital camera with $700nm$ bandpass filter.

4.2.1 Theoretical Analysis

A typical image for analysis is seen in Figure 4.1 (captured from a UNIQ 600CL digital camera with a bandpass filter centered at $700nm$, as discussed in Chapter 3). In Figure 4.1(a), the melt pool is fairly obvious, along with the difficulties labeled; namely reflection from the substrate, flares or plasma formation, and fuzzy/blurred boundary. In Figure 4.1(b), the main components in the process zone environment are highlighted, namely the solidifed clad, the substrate onto with the molten powder is being deposited, the laser beam, and the incoming powder stream.

As seen, the image is largely dominated by dark pixels, while the melt pool is relatively well segmented. This is more clearly demonstrated from the image's histogram, found in Figure 4.2. The melt pool is surrounded by a hazy region, where the thresholding algorithm must determine which pixels consist the foreground object (melt pool) or background object. This hazy region can also be seen in the histogram, represented by the pixel counts leading up to all white (255).

In Otsu's technique, a metric is devised which measures the inter-class variance.
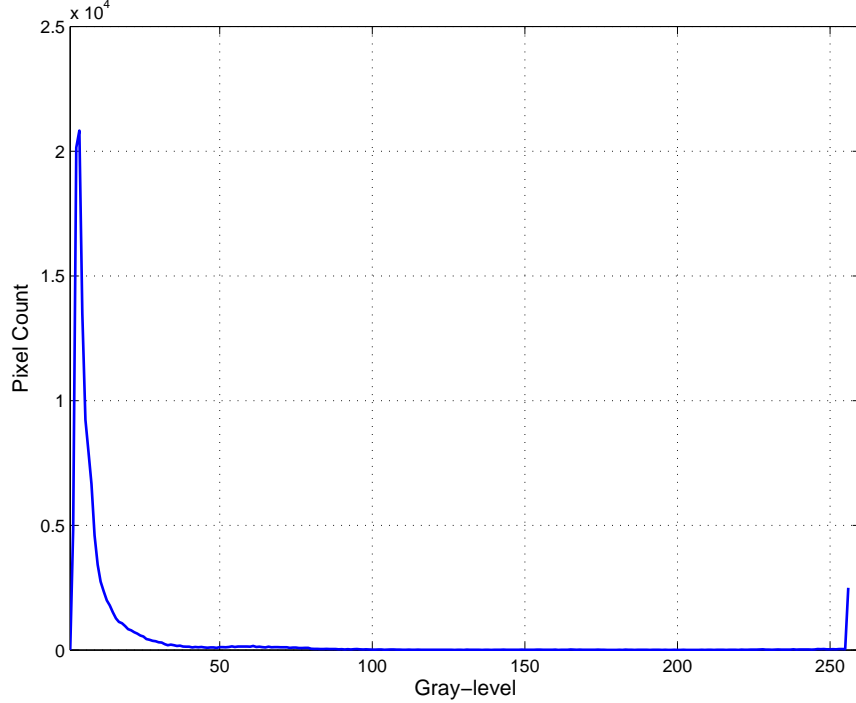
Figure 4.2: Histogram of typical process zone image, taken from 8-bit camera, or 256 gray-levels (see Figure 4.1(a) for image).

This metric is found below:

$$\delta^2 = (\mu_f - \mu_b)^2 (\omega_f \omega_b), \tag{4.1}$$

where μ_f and μ_b are the foreground and background means, respectively, and ω_f and ω_b are the probabilities of belonging to the foreground and background classes, respectively. These values are calculated by counting the number of pixels in each class. It can be seen that this metric will be largest when both the first and second terms are largest. The first term corresponds to the difference between class means, thus maximizing the distance between classes. The second term represents the product of the probabilities, and will be largest when the two terms are largest. The optimal threshold is found by going through all possible combinations of threshold values, calculating the metric of Equation (4.1) for each value, and then selecting the threshold of maximal inter-class variance.

The images captured by the digital cameras are mainly composed of three different regions: the actual melt pool, a hazy region around the latter, and the background. Due to the bandpass filter added to the digital camera's optics, the background is composed of very dark pixels, where no ambient light is captured. The melt pool however, is at the other end of the gray-scale spectrum, where it is mainly composed of very bright pixels. These two values create a very binomial distributed histogram, as shown in Figure 4.2. Otsu's technique thus divides the two peaks in the middle, and selects this as the optimal threshold. This allows for a large distance between class means (first term in the metric).

A second approach to calculating the optimal threshold is proposed by Huang and Wang [23], where a fuzzy algorithm to minimize the entropy of a given image is developed. The entropy E of an image X is measured by the following metric:

$$E(X) = \frac{1}{MN \ln 2} \sum_{g=0}^{L-1} S(\mu(g))h(g),$$

(4.2)

where the image X has dimensions $M \times N$, has L gray-levels, a histogram represented by the function $h(g)$, g being the gray-level, and $S()$ is Shannon's function, defined below:

$$S(y) = y \ln(y) - (1 - y) \ln(1 - y).$$

(4.3)

Also, in Equation (4.2), $\mu(g)$ is a function indicating the degree of membership of a given pixel to either the background or foreground region. This degree of membership is given by a Gaussian function, as:

$$\mu(y) = \exp\left[-\frac{1}{2}\left(\frac{y - T}{MAXGL \times \sigma}\right)^2\right]$$

(4.4)

where T is the possible optimal threshold, $MAXGL$ is the maximum gray scale value, and σ is a parameter to scale the width of the Gaussian function. This latter variable is left as a tuning parameter, however, the final threshold level is found to be rather insensitive to its value. It is set to $\sigma = 0.3$.

From these three equations, the procedure must first select a threshold value, and then compute the entropy of the image from Equation (4.2). This is repeated for

all threshold values, from $0 \rightarrow MAXGL$. The threshold value creating the lowest entropy for the image is the optimal threshold.

Looking back at the Otsu algorithm (Equation (4.1)), the goal is to maximize the metric δ^2, which is done by maximizing both the distance between the foreground and background mean values, along with the product of the probabilities of both the foreground and background. This last term will be greatest when half the pixels are classified as background, and the other half as foreground. This is not always desirable seeing as the melt pool can occupy only a small portion of the image, while the background the remainder. As a result, Otsu's technique would attempt to increase the number of foreground pixels to increase δ^2, which would result in the hazy region being included into the foreground; an unwanted result. In general, the thresholds obtained from this technique, applied to the images captured of the laser cladding process are around 50%, which allows the hazy region around the melt pool to be considered as a foreground object, which is unwanted.

On the other hand, the fuzzy algorithm utilizes the information from the histogram, as opposed to the probability of pixels. This information is combined with Shannon's function, which has minimal value for degrees of membership near 0 or 100%; maximum values are found for memberships around 50%. Thus, if a threshold is selected such that it is placed midway between two large clusters of pixels, their membership values will tend to be around 50%. However, if the threshold is placed very close to one cluster (resulting in a degree of membership approaching 100%), while far from the other (resulting in a degree of membership approaching 0%), Shannon's function will result in minimal values, thus producing minimal entropy. Since the majority of pixels have gray scale values near 0 (very dark images), and the fact that the histogram data is multiplied by Shannon's function within the summation, the algorithm should attempt to place the optimal threshold at a high gray scale value (near the white region). This will cause low degrees of membership for the great majority of pixels (since they are black pixels, and far from the threshold value), thus low values of Shannon's function, and as a result, would diminish the effect of high histogram values at low gray scale values. These combined effects should result in greater optimal threshold values, and thus eliminating, or at least greatly reducing, the addition of a hazy region around the melt pool in the captured
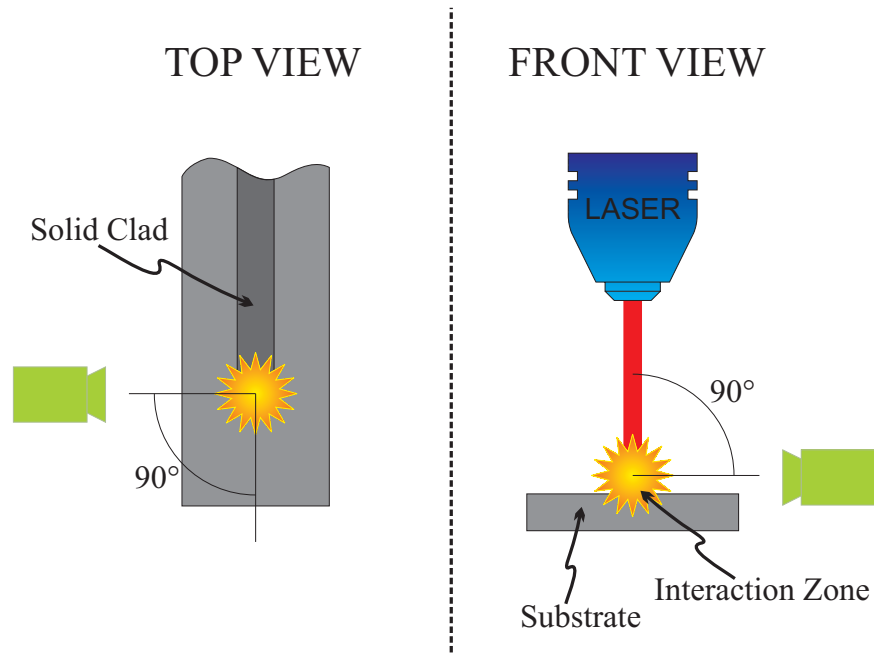
Figure 4.3: Position of camera with respect to melt pool. Camera is perpendicular to the direction of travel, and to the vertical plane. Images captured will be used to investigate two thresholding techniques.

images.

4.2.2 Experimental Setup

As discussed in the previous section, there exists a hazy region around the melt pool, which may be included into the real measured pool after thresholding. Thus, to evaluate each algorithm, it is decided to analyze the degree to which this hazy region is included in the thresholded image. For this, the true height of the deposited clad is compared to the height obtained from the thresholded images, captured from cameras perpendicular to the process (see Figure 4.3). Three experiments are conducted, where images are captured at 10 Hz from one digital camera (UNIQ UP-600CL), fitted with a bandpass filter centered at $700nm$.

To estimate the clad's height, the camera is placed perpendicular to the process, as previously mentioned, and shown in Figure 4.3. Clads are deposited in straight lines, and therefore, one can count the height of the clad in terms of pixels, for each
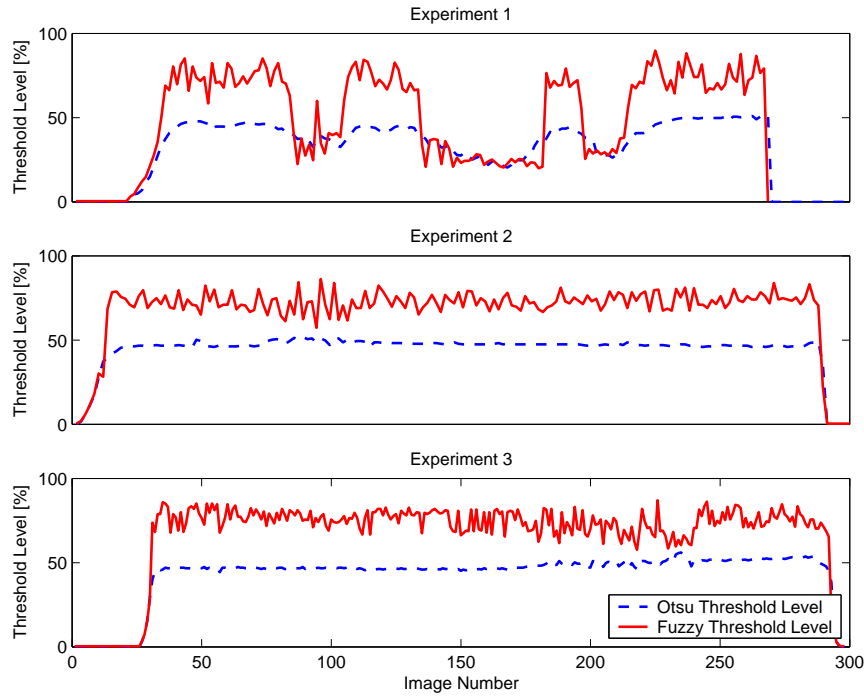
Figure 4.4: Threshold levels obtained through Otsu and a fuzzy algorithm methods for each image in the three experiments.

image. That is, counting from the heighest point on the segmented melt pool, down to the reference plane (or substrate), reveals the height in terms of pixels. Converting pixels into metric units can be done by capturing a picture of a ruler, and measuring the number of pixels per unit length. This is similar to the method for obtaining the clad's true height, as will be discussed in the following paragraph.

To measure the true height of the clad, the latter is placed under a microscope, where digital pictures are taken. These pictures are then analyzed offline, where the height of the clad is measured, in pixels. Using the microscope's magnification factor, the heights are then converted into millemeters. Typical resolutions obtained in this manner are $\sim 10\mu m$/pixels. See Appendix C for further details.

4.2.3 Results and Discussion

The results of applying the Otsu and fuzzy-threshold algorithms are presented in Figure 4.4 for all images captured during the three experiments. As can be seen, the fuzzy algorithm produces consistently higher thresholds than Otsu's technique (mean of $\sim$75%), for the last two experiments. In the first experiment, large pertubations to the process were reflected in drastic changes in the captured images, resulting in varied threshold computations for each technique. However, this ability of the fuzzy algorithm to consistently produce larger threshold levels greatly reduces the size of the hazy region around the melt pool.

The threshold obtained with Otsu's technique are very stable about a mean value of $\sim$50%, for the last two experiments. On the other hand, the fuzzy algorithm has larger deviations about its mean value, which indicate its ability to adapt to small changes in melt pool conditions.

To further investigate this feature, height estimates using each threshold algorithm are shown in Figure 4.5. The inclusion of this hazy region can clearly be seen in these results, as the height estimated based on Otsu's technique has a bias with respect to the true height. However, the height estimated based on the fuzzy algorithm's melt pool segmentation performs very well in estimating the true height, even though its threshold levels have larger deviations from the mean value. This good agreement illustrates its ability to ignore the hazy region by varying the threshold level based upon small changes in melt pool dynamics (reflected in changes of hazy region).

It should be noted that conditions do occur where both threshold levels result in bad estimates of the true height. These conditions can be attributed to process instabilities, whereby large amounts of light are irradiated towards the camera, causing larger than normal melt pools, with very little hazy regions. This can be seen in experiment 2, from 6-10mm along the clad.

As a last step, Figure 4.6 illustrates one image thresholded by both techniques under normal conditions. As shown in the original image, the hazy region is clearly seen. When applying the fuzzy algorithm, this latter region is no longer present, as opposed to the lower threshold value from the Otsu technique, which encompasses this light into the melt pool.
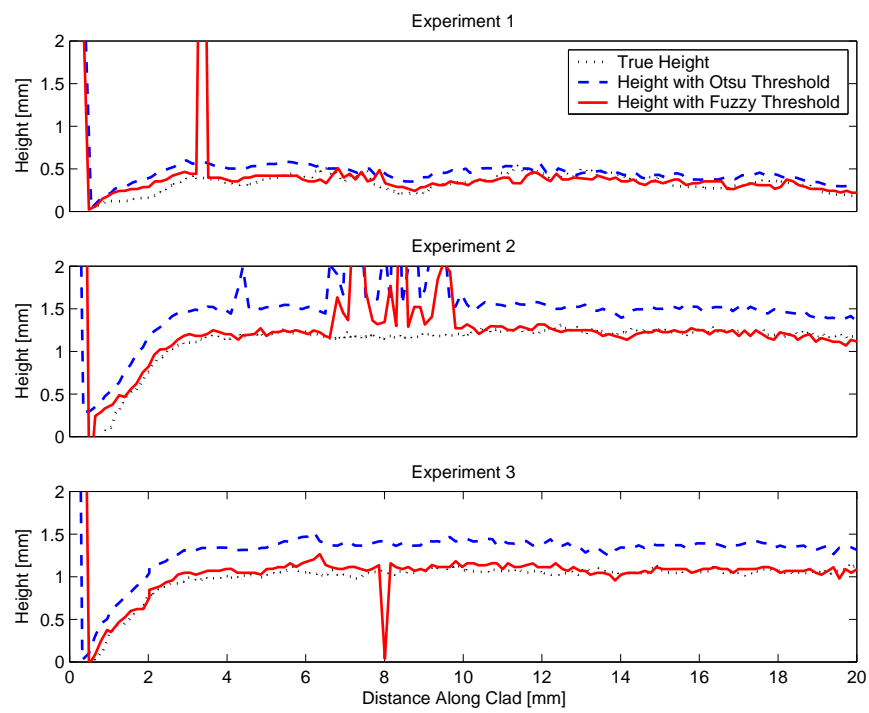
Figure 4.5: Estimate of clad height resulting from melt pools obtained with Otsu and a fuzzy algorithm thresholds. True height obtained offline, to an accuracy of $\sim 12\mu m$.
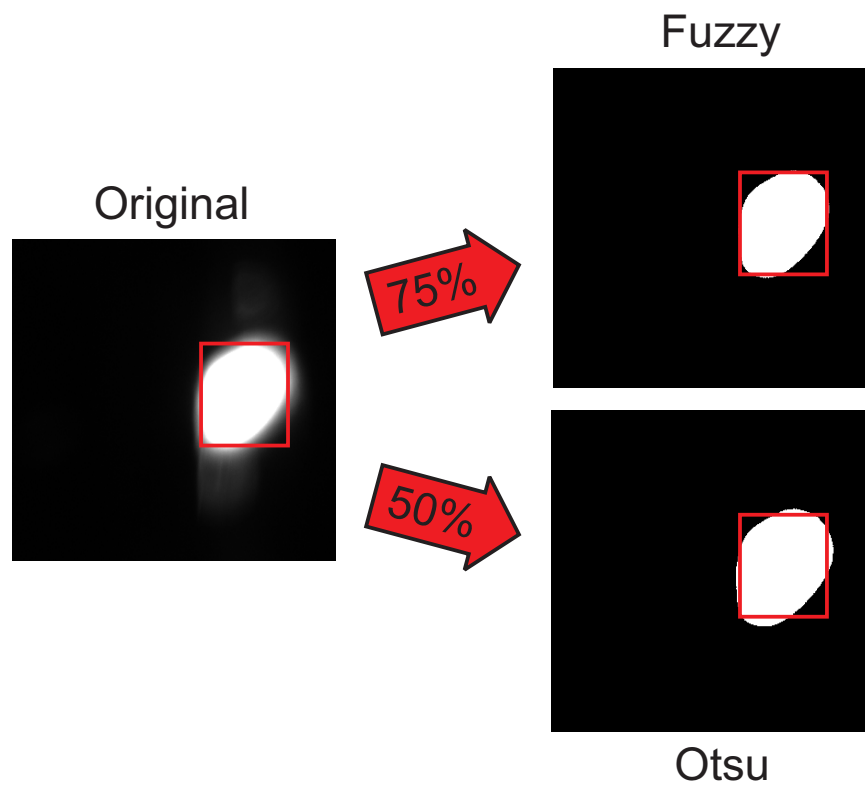
Figure 4.6: Sample image binarized by both threshold techniques. As seen, the hazy region around the melt pool is captured by Otsu's low threshold, as compared to that obtained from a fuzzy algorithm.
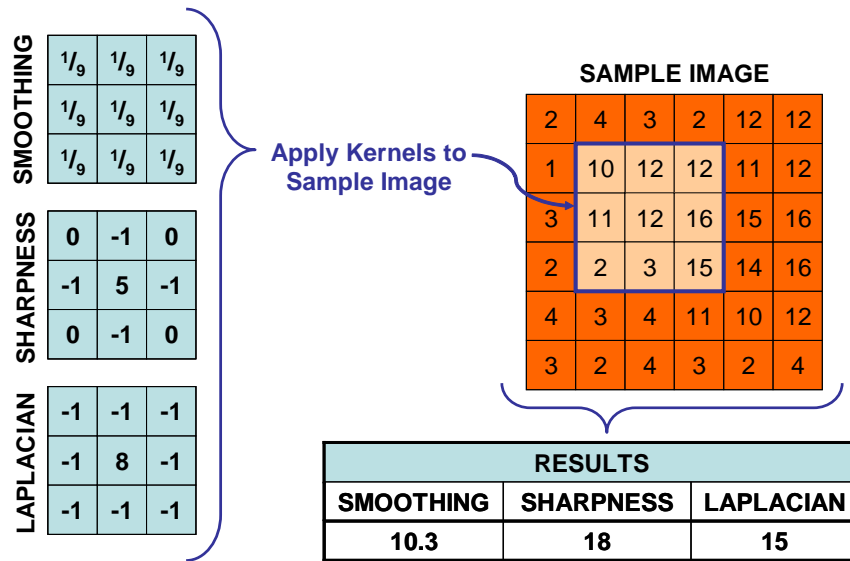
Figure 4.7: Example of kernel operations on a sample image.

4.3 Boundary Tracing

With a thresholded image, pixels have a value of either 1 (white) or 0 (black). A convention is adopted such that the foreground objects are white, while the background objects are black, and it is the former that one wishes to analyze. In the case of melt pool segmentation, it is desired to segment the border of this latter, which will then be used for further analysis.

Several techniques exist for finding the border of an object, and can be classified in two main categories: derivative-based and comparison-based. In the first option, a mask (or kernel) is placed over a neighborhood of pixels (such as 2×2, 3×3, 5×5, etc.) and the cumulative sum of the product of corresponding pixel and kernel entries is calculated. The result provides information of the pixels in this neighborhood, and is associated to the middle pixel over which the kernel is placed. For example, Figure 4.7 illustrates the algorithm for several typical kernels, namely smoothing, sharpness and Laplacian kernels.

Three common techniques utilize these kernels operations to detect edges, mainly from gray-scale images [24]. They can equally be applied to binarized images, as will be discussed. All three techniques compute the spacial gradient of the image at each

pixel location. If the gradient is sufficiently high (corresponding to a change in pixel values, which is characteristic of edges), then the pixel at which this spacial gradient is calculated becomes an edge, or boundary pixel. The level at which a gradient is considered an edge is predetermined, and used as a tuning parameter in the technique.

The first technique is referred to as a *Roberts* edge detection algorithm, and consists of two 2×2 kernels, one for each direction. This is illustrated in Figure 4.8(a). Both kernels are placed over a neighborhood, and the gradients in each direction (x-gradient G_X and y-gradient G_Y) are computed. They are then merged together into an overall spacial gradient G, in a geometric manner, stated in Equation (4.5):

$$G = \sqrt{G_X^2 + G_Y^2} \tag{4.5}$$

If this gradient goes beyond a predetermined threshold, the pixel over which the kernel is applied is considered as an edge, or boundary pixel.

The second technique is the *Sobel* edge detection algorithm, which relies upon the same computations as the Roberts operator, however, the two kernels utilized are of size 3×3, as illustrated in Figure 4.8(b). Again, both kernels are applied to a neighborhood, and the gradient in each direction is computed. The overall spacial gradient G is again calculated with Equation (4.5), and if this value goes beyond a predetermined level, the pixel is considered to be an edge, or boundary pixel.

The third technique is known as the *Canny* edge detection algorithm. This algorithm is more complex than the previous two, and involves three distinct steps: Gaussian smoothing, kernel convolution, and edge connection. The first step consists of applying a Gaussian smoothing operation to the image, which reduces the number of possible false edges, or smooths-out the edges for better detection. The second step is to apply a cross-kernel to the image, such as a Roberts kernel. This identifies the edge pixels. Last, these pixels are connected via an algorithm which travels along the edge to create a continuous border.

The advantage of gradient-based algorithms, such as Roberts, Sobel and Canny, is that they can be applied directly to a gray-scale image without the need of computing an optimal threshold. However, the disadvantage is that the border pixels are given for the entire image, and in the case of noise (such as flaring or plasma formation),

+1	0
0	-1

G$_X$

0	+1
-1	0

G$_Y$

(a) Kernels applied in Roberts edge detection algorithm.

-1	0	+1
-2	0	+2
-1	0	+1

G$_X$

+1	+2	+1
0	0	0
-1	-2	-1

G$_Y$

(b) Kernels applied in Sobel edge detection algorithm.

Figure 4.8: Kernels used in Roberts and Sobel edge detection algorithms.

several pixels that do not belong to the melt pool are identified. This adds another step in the procedure, which consists of labeling those pixels belonging to the melt pool, and those that do not. Another disadvantage is the order in which edge pixels are output. Border pixels arise in the order that the kernels are applied, and thus, can produce raster-type edges. In the next category of techniques, this order will be much better as the algorithm will more efficiently trace the border in a clockwise manner.

In the second type of border detection techniques, namely the comparison-based algorithms, a binary image is taken, and based upon comparisons of pixels, the melt pool border can be traced. The following algorithm is border tracing based upon 8-connectivity. This algorithm has two main steps: identify a border, followed by tracing this border. First, a pixel on the border must be determined. This can be

done by going through each row of the image until a white pixel has been found, as shown in Figure 4.9(a)[2]. With a border pixel identified, the algorithm proceeds by checking the pixels in the neighborhood for another border pixel, in a clockwise manner, as shown in Figure 4.9(b). When another pixel is identified, the direction of this identification is important as it defines the starting point for the next search of another border pixel. Tracing of the border continues until the original border pixel in the first step has been re-identified (Figure 4.9(c)).

Before continuing, it was mentioned that the direction upon which a border pixel is identified is very important. In order to prevent redundant identification of border pixels, and to properly follow the border, the next direction in which a neighborhood pixel is searched is shown in Figure 4.10, which is for 8-connectivity (hence the eight arrows)[3]. For example, in Figure 4.9(b), the first border pixel is identified as a result of an arrow pointing in Direction 1. It is now required to search in this pixel's 3×3 neighborhood for the next border pixel. Since we have come from Direction 1, we must begin searching the neighborhood at Direction 4, as prescribed in the look-up table of Figure 4.10. If this pixel is not a border pixel (as is the case in Figure 4.9(b)), then searching through the neighborhood continues, in an ordered clockwise manner, as shown in this figure. The next border pixel is identified at Direction 8, where the next pixel in this new border pixel's neighborhood will begin at Direction 3.

Comparing the border tracing techniques, the derivative-based methods require no thresholding of the image, however, do require more complex calculations at each pixel location (since addition and multiplication are performed). Also, the algorithm requires a given threshold level to determine if the gradient is sufficiently large to cause an edge, which can become subjective, especially with blurry melt pool borders. Finally, the output edges must be analyzed afterward to determine which are actual melt pool borders. On the other hand, the comparison-based technique requires computation of an optimal threshold, however, much less computation at each pixel location (since it is only a comparison operation), and outputs the border pixels in sequential order of the melt pool, in a clockwise rotation.

---

[2]An important modification to this is starting the search at the center of the melt pool, which greatly reduces the possibility of identifying a false border, such as flares or moltent powder particles in flight.

[3]4-connectivity also exists, whereby only 4 directions are used, and are separated by 90°.
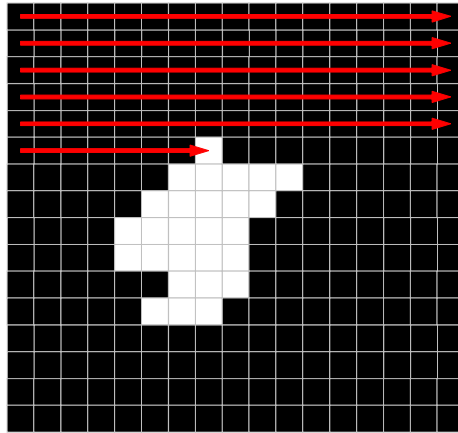
(a) Pixel identification in test image.
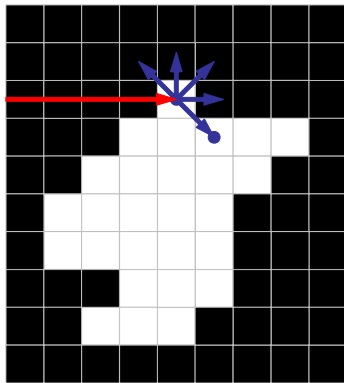
(b) Clockwise rotation for identification of next border pixel.
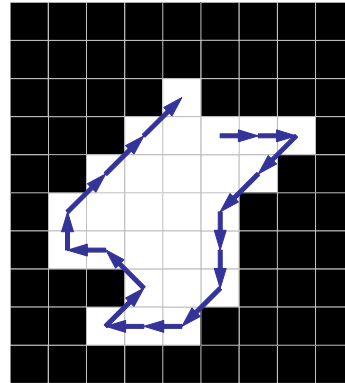
(c) Movement along border pixels.

Figure 4.9: Schematic of 8-connectivity border tracing algorithm used in segmentation of melt pool from binarized image.

Requiring calculation of an optimal threshold is comparable to the last step of border pixel identification of derivate-based methods, and therefore both can be ignored. As a result, the second technique is much quicker than the first at each pixel location (since only comparisons are performed, as opposed to addition/multiplication operations). For this reason, the second technique will be used in providing melt pool border coordinates. In addition, this allows the threshold algorithm decipher the melt pool's blurry boundary, as opposed to tuning the predetermined level at which a gradient is considered to be an edge.

Current	Next
1	4
2	5
3	6
4	7
5	8
6	1
7	2
8	3
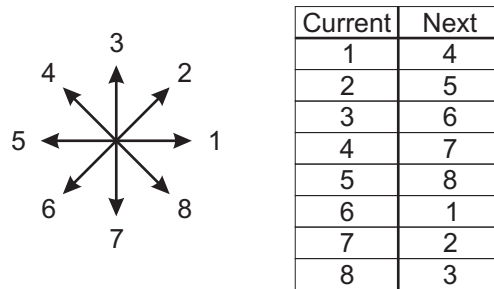
Figure 4.10: Next search direction based upon current direction. The current direction corresponds to the direction which has correctly identified a border pixel. The next direction identifies the neighborhood pixel which is searched next for the following border pixel. This prevents redundant identification of border pixels, and correct tracing of the border.

4.4 Conclusions

The first part of melt pool segmentation consists of binarizing the captured image. That is, an optimal threshold is selected such pixel values beneath are considered as background objects (value of 0), and pixel values above are considered the melt pool (value of 1). Two techniques were investigated for calculating this optimal threshold: Otsu's method and a fuzzy-algorithm. Although the melt pool is well segmented with the human eye, there does exist a hazy region around its border, which causes the most problems for threshold algorithms.

Otsu's method consisted of maximizing inter-class variance. That is, a metric was calculated for each possible threshold level (see Equation (4.1)), and the latter with the greatest metric was selected as the optimal threshold. Maximizing this metric was accomplished by having an even number of pixels in each class, along with maximum distance between the two. Due to the high number of dark pixels, a low threshold level is taken such that an even number of pixels are in each class, however, this includes the hazy region around the melt pool into the foreground object, which is unwanted.

The fuzzy algorithm was based on minimizing the image's entropy, after binarization. That is, the image's entropy is calculated for all possible threshold levels (see Equation (4.2)), where the lowest value is taken as the optimal threshold. Minimization of the image's entropy is achieved through low products of Shannon's function and histogram information. Due to the high number of dark pixels, this is done by

placing the optimal threshold at a high level, which is desired as it reduces the amount of hazy region captured in the melt pool.

Three experiments were conducted to quantitatively compare the algorithms. The thresholds computed with Otsu were consistently lower than ($\sim$50%) those obtained through a fuzzy algorithm ($\sim$75%), as expected. This predicted a larger hazy region for Otsu images. To verify this, the height of the segmented melt pools were measured to obtain an estimate of the true height, whereby Otsu estimates provided consistenly biased estimates, as opposed to fuzzy-based estimates which had little error. The Otsu thresholds were much more stable than fuzzy, however, this prove to be inadequate as it always incorporates the hazy region. Meanwhile, the larger deviations of fuzzy thresholds about its mean value enabled the latter to adapt to changes in melt pool sizes, and thus hazy regions.

After binarizing the image, melt pool's boundary must be extracted. Two types of techniques are discussed: derivate- and comparative-based. Derivative-based techniques require more calculations at each pixel location, since a spatial gradient is being computed. Also, border pixels arrive in raster-order. On the other hand, much less computation is required at each pixel location for comparision-based techniques, and border pixels are output in a more convenient order, as the algorithm traces the border. For these reasons, the melt pool is extracted for a binary image through a comparative technique based upon 8-connectivity.

Chapter 5

Feature Extraction: Clad Height

5.1   Introduction

In the previous chapter, the boundary of the melt pool was segmented from the image captured by the digital camera. This boundary represents the silhouette of the melt pool, as seen by the camera's perspective. From this boundary, it is desired to extract the height of the clad currently being formed. To extract this feature from the melt pool silhouette, three possible techniques are considered: 3D reconstruction, shape from silhouette, and a shadow analysis. The first technique utilizes common traits in multiple camera images, along with triangulation of their data, to reconstruct a 3D model of the object in question (i.e. the melt pool). This assumes no predefined shape of the melt pool. The second technique assumes a predefined shape for the melt pool, and using the boundary (or silhouette) of the melt pool, recreates this assumed shape from multiple images. In the third technique, the camera is assumed to be a source of light, whereas the projection of the silhouette from the image plane onto a work plane is considered as the object's shadow. This shadow is then analyzed in the aforementioned work plane to estimate a height causing this shadow. Each technique will be further discussed in the following paragraphs.

The first technique, 3D reconstruction, requires the use of two or more images taken from different positions with respect to the melt pool. The technique recon-

structs the shape point-by-point, where point correspondence[1] between images outputs a mesh of coordinates of the melt pool's outer surface. This is accomplished by identifying common points on the melt pool in multiple, separate images. With the common point's coordinates in multiple images, one can determine the three-dimensional coordinate in the workspace with triangulation.

The main advantages to this technique are that no predefined shape of the melt pool is assumed and, the end result is a three-dimensional shape of the melt pool's outer surface. This allows for full geometrical properties to be measured, such as width, height, angle of solidification, etc.

However, two major difficulties arise: observability and point correspondence. Observability is the criterion for which a surface may be reproduced if it is observable by two or more cameras [25, 24, 26]. That is, only areas of the melt pool seen by two or more cameras may be reproduced. The main problem arises from self-occlusion, where one camera can see one side of the melt pool, while another camera is orientated such that it can see the other side. This requires the cameras be properly positioned and orientated such that a large region is common to all cameras. Solving this, point correspondence represents a larger problem. Point correspondence refers to the task of identifying a common point in the real world to its location in multiple images. That is, how does one go about identifying the exact point in more than one captured image? This is an ongoing problem in the field of Computer Vision. With basic shapes, such as cubes or walls, the intersection of lines can provide useful information [26]. Also, utilizing the epipolar constraint placed upon a set of multiple cameras can reduce the size of the region where pixels must be analyzed [24, 27, 26]. Many successful techniques use histogram information [26], where it is assumed that a point on the object has the same light intensity in all images. The major problem in applying this technique to the melt pool images is the lack of histogram information. Typical images of melt pools are largely black-and-white, and have very little gray pixels[2]. Thus, matching points based upon light intensity is very difficult.

---

[1] Point correspondence is the process by which a point in the real world is recognized in all images. That is, the point can be seen and identified in all images as the same point in space.

[2] It should be noted that increasing the resolution of the camera could help this situation. That is, images only have 8-bits of data per pixels, thus 256 gray levels. Increasing this to 10-bits could potentially address this issue of black-and-white images.

The second available technique for feature extraction is to reconstruct a predetermined melt pool shape based upon silhouettes observed from multiple images. The key to this method is that a predetermined, or assumed three-dimensional shape is given to the melt pool. From this assumed model, theoretical silhouettes seen by each camera can be determined, based upon camera orientation with respect to the melt pool. This last step is the major drawback of the technique. The silhouette seen by each camera can change both due to melt pool size (i.e. height), and due to the tangential direction of the clad being deposited. It therefore becomes difficult to determine whether the silhouette has changed as a result of the height changing, or the clad's tangential direction. One possible solution is to determine the theoretical silhouette for all possible tangential directions through experimentation. This, however, requires a large amount of empirical curve fitting for an assumed shape.

The third and final technique for feature extraction is done by analyzing the melt pool's shadow. This shadow is obtained through the perspective transformation of the melt pool's silhouette, from the image plane to the horizontal world plane. With the shadow of the melt pool in the world plane, the problem becomes much simpler, as the height is a function of the length of the shadow. Making basic assumptions, this relationship can be given by trigonometric theorems of right angle triangles. The difficulty in this approach lies in the measurement of the shadow's length, as the clad's formation is dynamic, where its solidified height can be at an unknown distance from the reference origin.

It now remains to decide upon a technique, based on the descriptions above. The first technique, 3D reconstruction, can be eliminated immediately as the problem of point correspondance is enormous when considering the information given in a melt pool image. Since the melt pool is essentially white pixels, and the background is covered with black, there is very little information to gather from the grayscale values, hence rendering most point correspondence techniques ineffective. The second technique, shape from silhouette, requires one to assumed a predefined shape for the melt pool. This is rather difficult as a melt pool is formed by liquid metal, which is free-flowing and has no specific shape. In the majority of cases, the melt pool shape is somewhat constant, however, even with a well defined shape, it would take a large number of experimental data to empirically associate clad height to a

silhouette, especially if it is desired to have independence from the deposition path. This leaves the last technique, estimating height from the melt pool's shadow. This technique assumes that the melt pool's boundary, as viewed in the image plane, can be transformed to obtain an equivalent shadow of the latter. If this is possible, then it only remains to determine the origin of this shadow, which should be a good approximation to the clad's solidified height. Therefore, the first two techniques will be placed aside such that the third method of height estimation can be further investigated.

5.2   Theoretical Analysis

In this section, two algorithms will be developed based upon the perspective transformation of the melt pool's shadow onto a work plane. In the first algorithm, two cameras are used to view the melt pool from different angles. The silhouette from each camera is projected onto the same work plane, whereby the width is extracted. From the width, and assuming a specific cross-section for the clad, one can obtain an estimate of the height. Due to practical problems (as will be further discussed), a second algorithm is developed which makes different assumptions and relies upon more stable regions of the melt pool. This algorithm produces relatively good estimates, however leads to the development of a third technique, which does not rely upon any perspective transformations.

Each algorithm will be further discussed in the following sections, with results shown in Section 5.4. However, before proceeding, the perspective transformation will be developed as it is common to the first two techniques.

5.2.1   The Perspective Transformation

A perspective transformation is used to convert a two-dimensional point from one plane to another [27]. In order for this transformation to occur, the 2D point must

be placed into a homogeneous representation, namely

$$\underbrace{\begin{pmatrix} x \\ y \end{pmatrix}}_{\text{Cartesian Coordinates}} \rightarrow \underbrace{\begin{pmatrix} x \\ y \\ 1 \end{pmatrix}}_{\text{Homogeneous Format}} = P_0.$$

In this format, one can define the perspective transformation of a point P, from plane 0 to 1, as:

$$P_1 = \mathbf{H} P_0, \tag{5.1}$$

where P_0 is defined above, P_1 is the resulting 2D point in the new plane, and $\mathbf{H}$ is a homogeneous transformation matrix. This transformation matrix is defined up to scale [27], resulting in eight unknown parameters:

$$\mathbf{H} = \begin{pmatrix} a & b & c \\ d & e & f \\ g & h & 1 \end{pmatrix} \tag{5.2}$$

The $\mathbf{H}$-matrix is specific to a desired transformation. That is, it uniquely defines the transformation from one plane to another, and cannot be used for transformations into any other plane. A schematic of the transformation is shown in Figure 5.1. Amongst other things, the homogeneous transformation matrix defines a focal point from which all perspective rays originate (labeled as 'Camera Center' in Figure 5.1). With this is mind, it can be seen that transforming the silhouette of an object from plane 0 into plane 1 represents a shadow in this second plane. That is, if the source of light is at the focal point, then the object's shadow in plane 1 is found by a perspective transformation of the object's boundary in plane 0.

In the case of melt pool images, the latter's border is projected onto a horizontal plane, coincident with the substrate onto which it is being deposited. Thus, from a global perspective, the camera can be seen as a source of light whose rays cast a shadow of the melt pool onto the work plane. This shadow is directly related to the height of the object, or in this case, the melt pool.

It was briefly mentioned that the homogeneous transformation matrix has eight
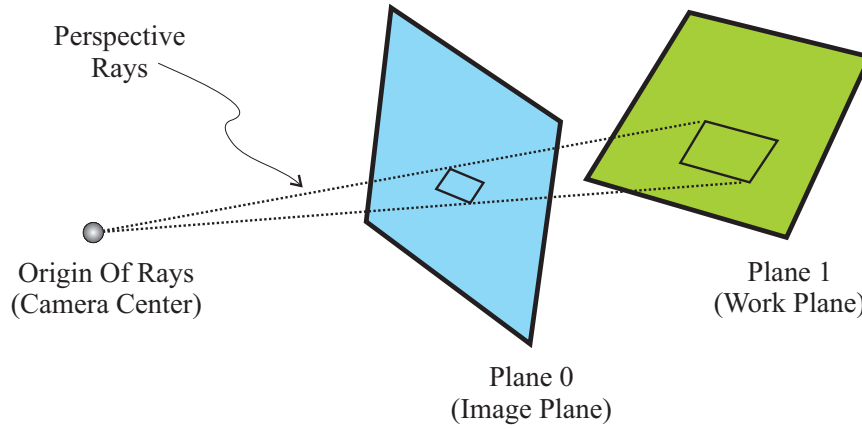
Figure 5.1: Perspective transformation from image plane to work plane.

unknown parameters, which uniquely define the transformation from one plane to another. To solve for the unknowns, a minimum of 4-points are required for an exact solution (it is preferred to have more points, such that a least-squares optimization can be performed). Points are placed on the work plane, where they are identified in the image plane (supplied by the camera). The correspondence of points enables one to uniquely solve for the transformation matrix between these two planes. See Appendix A for a detailed derivation of the solution.

5.2.2 Algorithm 1: Intersection of Two Projections

The first algorithm is based upon the perspective transformations obtained from two independent views of the same melt pool[3] . These views are obtained from two identical cameras orientated 120° apart. Due to this angle of separation, each camera is capable of witnessing a different side of the melt pool, as shown in Figure 5.2. Thus, the projection from one camera will see one edge of the melt pool's interface with the substrate, while the other camera will see the other intersection, on the other side of the melt pool. This allows one to determine the width of the clad being deposited.

Figure 5.3 shows a top view of the melt pool border's projection, as seen by each camera. A cross-sectional view of the clad is also shown, illustrating how the width W of the clad can be extracted from the projections. The remainder of the information

---

[3]This algorithm is partially based on the work done in [28].
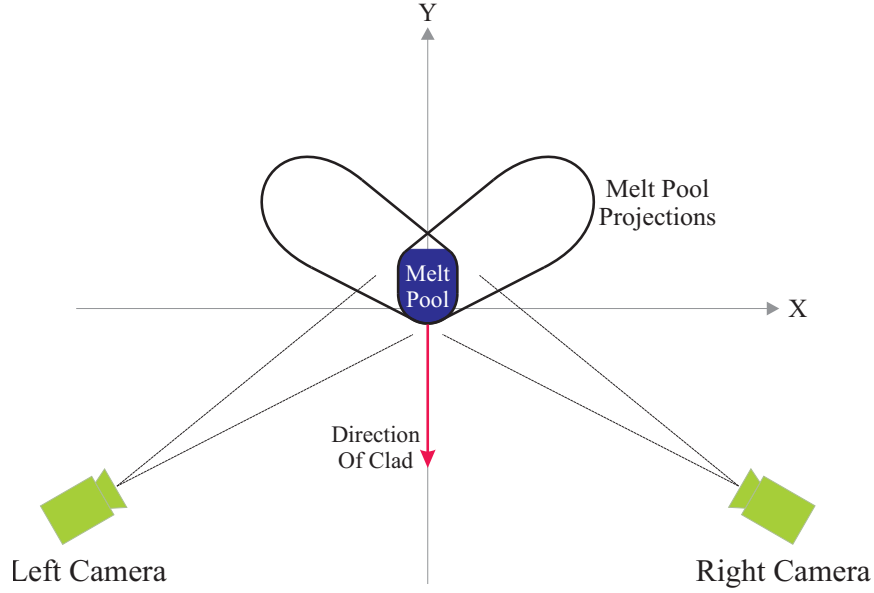
Figure 5.2: Schematic of camera setup for Algorithm 1. Due to their orientation (120° apart), each camera is capable of viewing one side of the melt pool. It is therefore straightforward to measure the clad's width from the projections.

provided by the projections relates to the shadow created by the compound angle of the camera with respect to the melt pool.

Assuming a specific cross-section for the clad, and combining the length of the shadow S with the angle of the incoming perspective ray, α, one can obtain an analytical solution to the height of the clad. Inherent in this development is the tangency of the perspective ray to the clad's cross-section, occuring at a point (x_t, y_t). Assuming a parabolic cross-section, this point is defined as

$$
\begin{aligned}
x_t &= S + W - \sqrt{S^2 + 2SW} \\
y_t &= \sqrt{S^2 + 2SW} \tan(\alpha).
\end{aligned}
\tag{5.3}
$$

where S, W and α are shown in Figure 5.3, with subscripts indicative of the camera from which the information is gathered. Using this information, the clad's height (*i.e.* height of the assumed parabolic cross-section), is given by:

$$
h = \frac{W^2 \tan(\alpha)}{2x_t}.
\tag{5.4}
$$
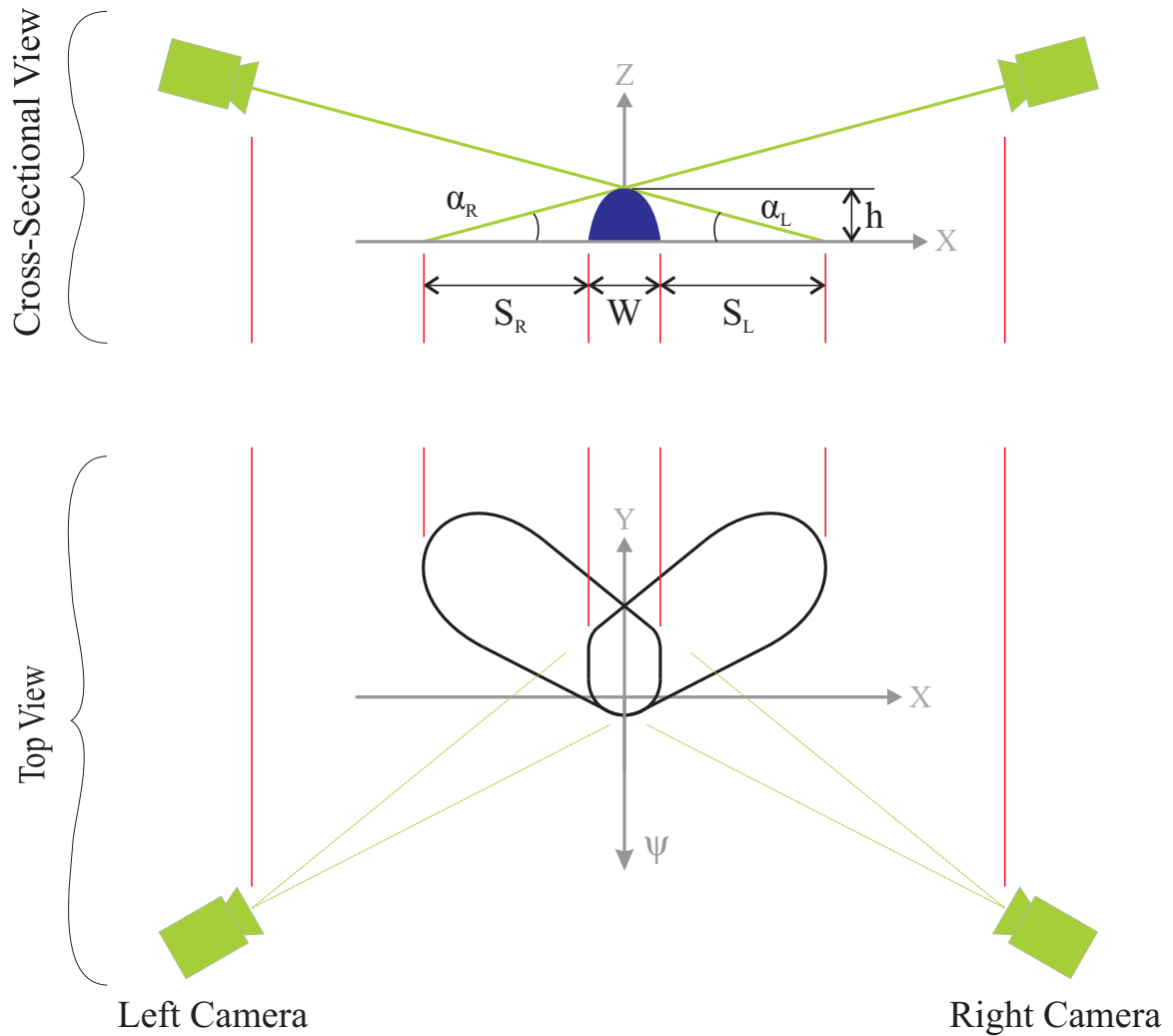
Figure 5.3: Detailed schematic of Algorithm 1. Width of clad is determined from projections of both cameras.

It is shown in Figure 5.3 that two shadow lengths can be obtained, (S_L, S_R), one for each camera. To combine the information from the two cameras, a final height is obtained by averaging the result from each camera.

It should be noted that the previous is developed for a clad whose tangential direction ψ bisects the cameras. If ψ deviates from this direction, the shadows projected from each camera will have different lengths, however, should result in the same height. Since the camera angle α does not change, it remains that this shadow

length must be adjusted. The algorithm is first tested whereby ψ does bisect the two cameras, to validate the previous theory.

In testing the algorithm for a bisecting ψ, it is noticed that the clad's cross-section does not remain constant. That is, the cross-section varies both within an experiment, and from experiment-to-experiment. The cross-section is a good sign of clad quality, in terms of diffusion with the previous layer. A parabolic cross-section represents ideal diffusion, where the wetting-angle[4] is small. However, the wetting-angle often becomes very large, indicative of a circular cross-section, and poor diffusion with the previous layer.

Different cross-sections result in different measures of the clad's width. Figure 5.4 illustrates this with two widely different cross-sections. In Figure 5.4(a), a typical, ideal cross-section results in the proper extraction of the width feature. However, if diffusion is poor (resulting in a greater wetting-angle), the width measurement suffers, as shown in Figure 5.4(b). With a poor width measurement, the analytical solution of Equation (5.4) yields a false height.

Although it is desired to have ideal diffusion with the previous layer (or substrate), it is not always the case. In spite of this, the height algorithm should continue to provide a good estimate. For this reason, a second technique is developed, placing less emphasis on the clad's cross-section, and more upon the shadow's length.

5.2.3 Algorithm 2: Shadow Length of One Projection

In this section, the author develops novel algorithm, where less dependence is placed on the clad's cross-section, but rather, on the shadow length. The algorithm assumes no specific cross-section for the clad; instead, the camera is assumed to be a light source, whereby each pixel in the melt pool is considered as a straight pole. By projecting a point from the image to the work plane (substrate), one can measure this shadow length and knowing the origin of the light source (or camera), the height can be estimated from a simple right-angle triangle.

To illustrate this concept, imagine a cube resting on a surface, with a distinctive shadow outline, as shown in Figure 5.5. The cube's height $\left|\overline{AB}\right|$ is related to the

---

[4]The wetting-angle is a measure of the angle formed by the clad's cross-section when intersecting the substrate (or previous layer). It ranges from 0 to 180°.

(a) Parabolic Cross-Section.

(b) Circular Cross-Section
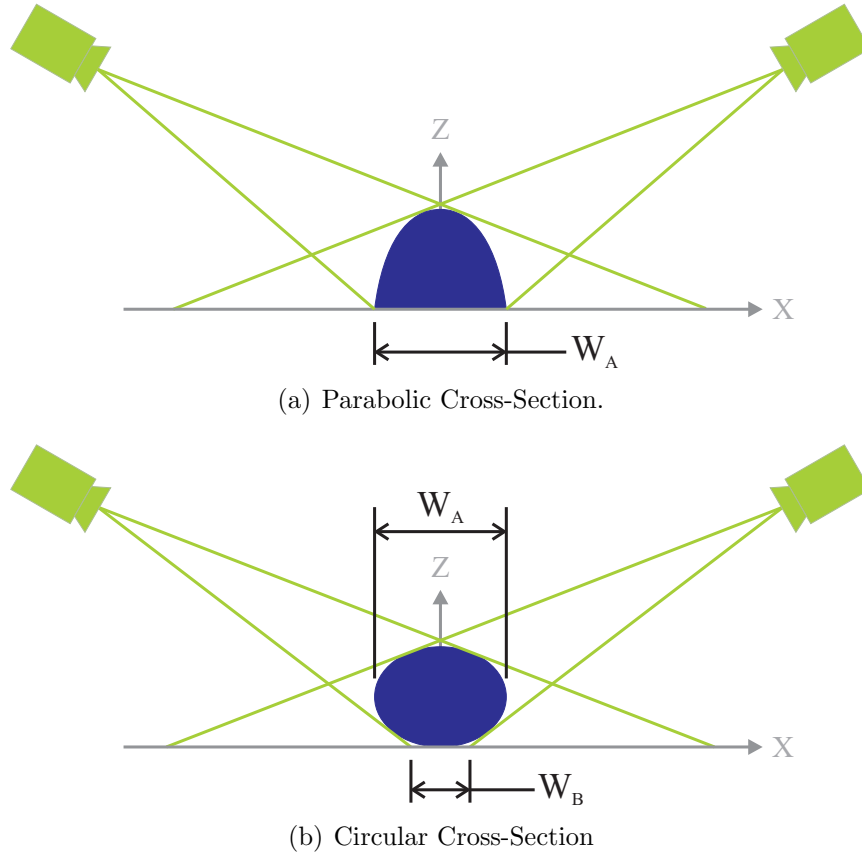
Figure 5.4: Effect of various cross-sections, all having the same width, but different wetting angles.

shadow's length, $\left|\overline{BC}\right|$, by the tangent of the angle $\angle ACB$. More formally,

$$\left|\overline{AB}\right| = \left|\overline{BC}\right| \tan(\angle ACB) \tag{5.5}$$

When applied to the melt pool images, the camera's focal point is considered the source of light, and the projection of the border onto the substrate is the shadow. It remains to ensure that the projection represents the actual shadow. For this, the picture of a $2mm$ cube is taken from a camera elevated at 15° to the surface. The border of this cube (outlined in Figure 5.6(a)) is projected onto the substrate, shown in Figure 5.6(b). The height at different points is estimated based upon Equation (5.5). The height estimated at points B, G, and F is calculated as $1.93mm$, $2.05mm$,
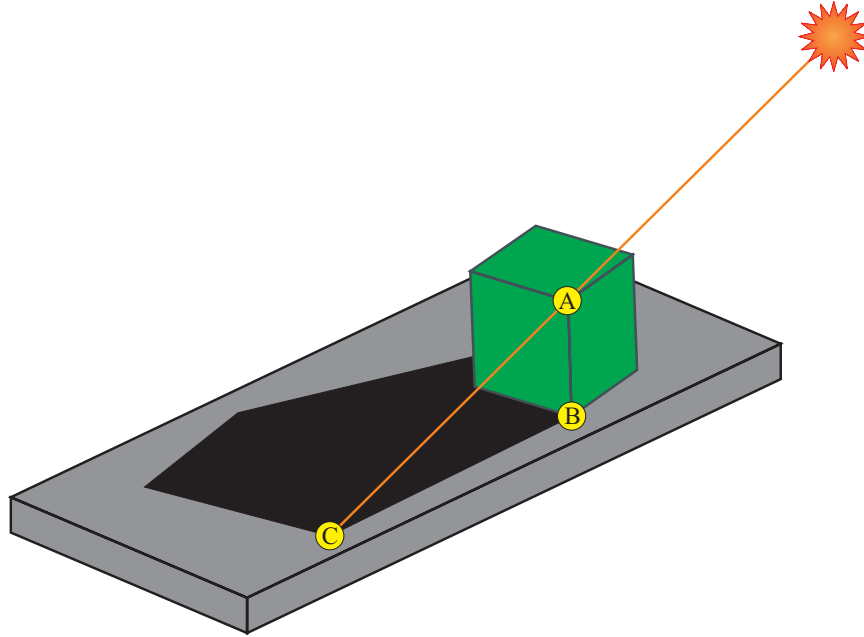
Figure 5.5: Schematic of principle upon which Algorithm 2 is based. The height of the cube (length of segment AB) is related to the shadow (length of segment BC) by the tangent of the angle ACB.

and $2.00mm$ respectively. This represents a very good estimate of the height, and verifies that the border's projection represents the object's shadow.

In this example, the shadow's length is measured from the projected point (c, d, or e) back to a location where the height is associated (b, g, or f, respectively). This shadow forms a segment which is parallel to the camera's line of sight. This shadow segment is crucial in estimating clad heights, specifically the location where the height is assumed.

Figure 5.7(a) illustrates a melt pool's longitudinal section, parallel to the direction of motion, ψ. Due to varying heat transfer rates, different solidification rates occur, causing the interface between liquid metal (melt pool) and solidified clad to be tilted. In addition, since the substrate is moving, the clad's actual, solidified height occurs at the top, right-most point of the clad[5]. The offset from the laser's center-point (Z-axis), namely δ_o, is where the height occurs. Figure 5.7(b) illustrates a top-view of the same melt pool where the offset is shown with respect to the laser's center-

---

[5]This is assuming the substrate's velocity is directed to the left.
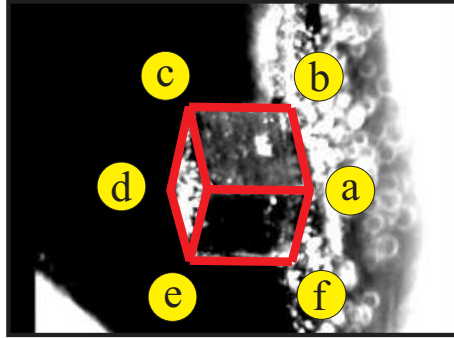
(a) Original picture of cube, where the outline represents the border to be projected onto a work plane.
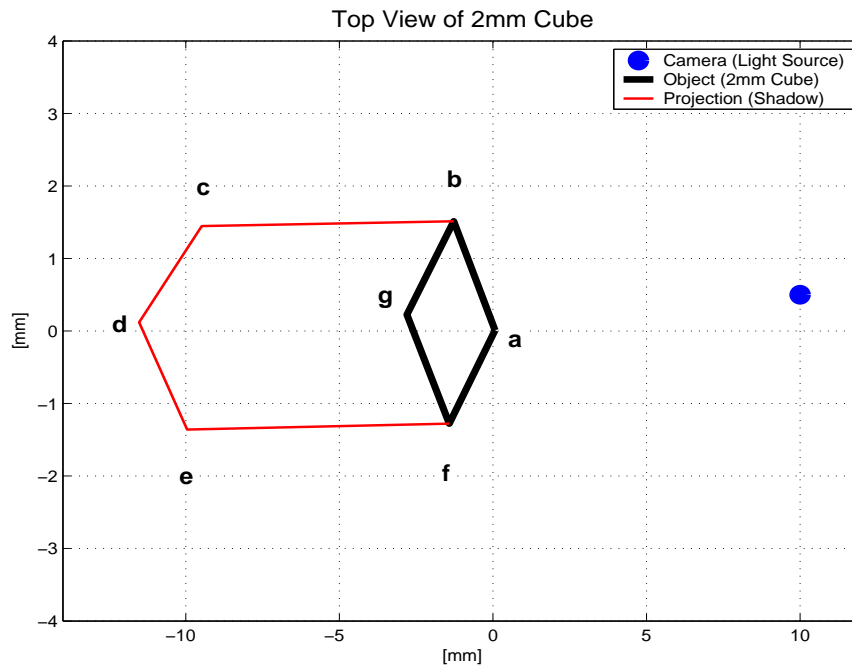
(b) Top view of cube. Black lines represent the cube, while the red represent the projected border from the original image. Points *c*, *d*, and *e* are shown in original image.

Figure 5.6: Estimation of cube's height ($2mm$) using length of shadow. Camera is elevated 13° from the work plane, onto which the shadow is projected. Height estimate at points *b*, *g*, and *f* are 1.93, 2.05, and 2.00mm, respectively.
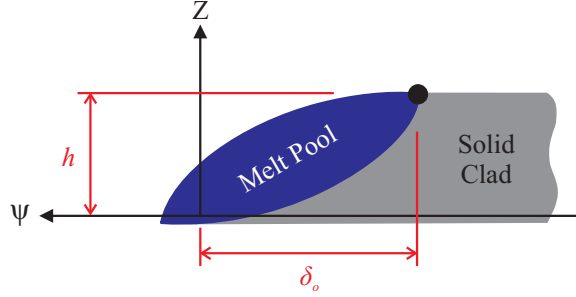
(a) Longitudinal section of melt pool, parallel to direction of motion, ψ.
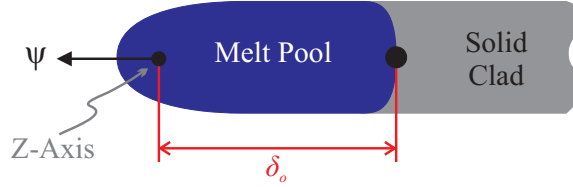
(b) Top view of melt pool, coincident with work plane.

Figure 5.7: Location of melt pool's height from two different perspectives. Height is at an offset δ_o from the laser's center point (Z-axis), along the direction of motion, ψ.

point (Z-axis). This view is very important since it coincides with the work plane (or substrate), which is the plane onto which the melt pool border will be projected.

The location of clad height is now determined as being at a distance δ_o from the laser's center-point, in the direction of motion ψ. It now remains to determine the length of the shadow, which is given by the projection of the melt pool's border in the image plane. Figure 5.8 shows a top-view schematic of the proposed shadow length measurement. Point Q represents the location on the clad where maximal height occurs, while point R is the laser's center-point at $(0,0)$. Therefore, it can be written that,

$$\left|\overline{RQ}\right| = \delta_o \tag{5.6}$$

and point Q is given as

$$Q = \left(\delta_o \cos\left(\pi + \theta_\psi\right), \delta_o \sin\left(\pi + \theta_\psi\right)\right) \tag{5.7}$$
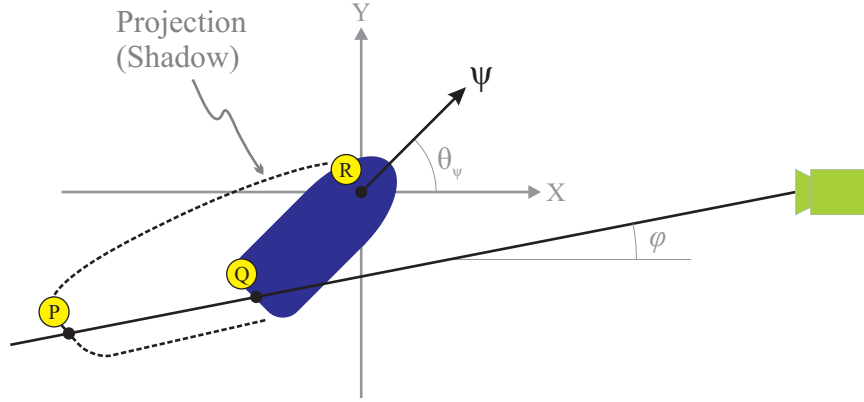
Figure 5.8: Schematic of Algorithm 2 and pertinent variables, namely the shadow (length of segment QP) location of maximum height (point Q).

as also shown in Figure 5.8. The dashed-lined represents the projection of the melt pool border from the image plane to the work plane. Drawing a line from the camera's focal point and through Q yields, point P on the melt pool's projection. This latter point represents the end of the shadow segment, while point Q is the height causing this shadow. Thus, the shadow length S of the clad's maximal height can be expressed as:

$$
\begin{aligned}
S &= \left|\overline{QP}\right| = \left|\vec{P} - \vec{Q}\right| \\
&= \sqrt{(P_x - Q_x)^2 + (P_y - Q_y)^2} \\
&= \sqrt{(P_x - \delta_o \cos(\pi + \theta_\psi))^2 + (P_y - \delta_o \sin(\pi + \theta_\psi))^2}
\end{aligned}
\tag{5.8}
$$

As with the $2mm$ cube, the height at point Q can be found with Equation (5.5) as:

$$
\begin{aligned}
h &= S \tan(\alpha) \\
&= \sqrt{(P_x - \delta_o \cos(\pi + \theta_\psi))^2 + (P_y - \delta_o \sin(\pi + \theta_\psi))^2} \tan(\alpha)
\end{aligned}
\tag{5.9}
$$

where α is the angle of the camera with respect to the work plane (or substrate). Therefore, for every melt pool image, one must determine the coordinates of point Q, subsequently allowing point P to be found, followed by the clad's height at this former point.

In Equation (5.9), all parameters are known with confidence, aside from δ_o. As previously discussed, the clad's height is at an offset δ_o from the laser's center-point,

along the direction of motion ψ. However, it was not mentioned that this offset varies with substrate velocity. With a higher velocity, the heat transfer rates are faster, creating a shorter clad. In turn, δ_o equally becomes shorter. With a slower substrate velocity, the opposite is true, whereby δ_o becomes longer. Thus, $\delta_o = f(v)$, with v being the substrate's velocity. Since this offset is used to locate point Q in the work plane, it will be further investigated.

Conducting experiments where the clad's direction of motion is perpendicular to the camera's line of sight ($\theta_\psi = 90^o$ while $\varphi = 0^o$, *i.e.* experiment 4 from Table 5.1) reveals images very similar to Figure 5.7(a). From these, the offset δ_o is measured for various velocities. The results indicate a parabolic relationship, as shown in Figure 5.9. The fit appears to be rather good, with an RMS of 3.1×10^{-4}. However, when looking at the standard deviation from the mean values (represented by the error bars at each velocity), it is seen that there are large deviations at each velocity. This may be indicative of noisy measurements within the melt pool's boundary, or subtle velocity changes that were not measured. In either case, it demonstrates how dynamic the melt pool is, making it difficult to accurately model the relationship $\delta_o = f(v)$. For this reason, it is difficult to estimate the position of point Q in Figure 5.8, which makes it even more difficult to locate point P. Therefore, it is necessary to devise another method for finding this latter point on the projected melt pool border.

An alternate method for finding the shadow point P is found by analyzing the border of the melt pool in the camera's image plane. In Figure 5.10, four images are shown, whereby β represents the angle between the camera's line of sight and the clad's tangential direction of motion, ψ. Also, the world coordinate system is shown (x, y, z), as seen by the camera. Based upon expert knowledge, the bold square represents the location of maximum height of the clad. When this point is projected, it represents point P. This point can thus be found in the image plane by simply measuring the height of all border pixels, in the z-axis direction. This is expected since the axis is normal to the surface.

With this point selected in the melt pool image, it is now transformed into the work plane through the perspective transformation of Equation (5.1). In the work plane, the shadow is still measured as the length of segment $\overline{QP}$, however, point Q is found by using the bestfit curve shown in Figure 5.9. Although this is an estimation,
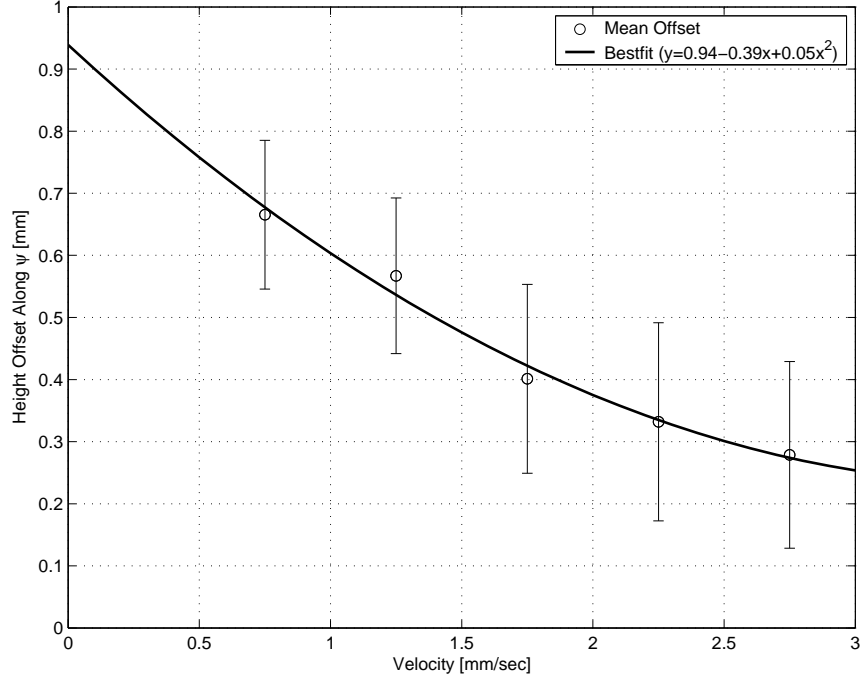
Figure 5.9: Mean value of offset measured along direction of motion, for various substrate velocities.

less error is induced since point P is found independently. The final algorithm is summarized in the following five steps:

1. In the image plane, measure the height of all points, in the direction of the z-axis. The highest point represents the location of maximum clad height.

2. Project this point onto the work plane with the perspective transformation of Equation (5.1), which yields the coordinates of point P.

3. Calculate the location of point Q in the work plane. This point is located along the direction of motion ψ, at a distance of δ_o. This offset has a parabolic relationship with respect to the substrate's velocity, as shown in Figure 5.9. The final coordinates are given by Equation (5.7).

4. With the coordinates of points P and Q, calculate the shadow length according to Equation (5.8).
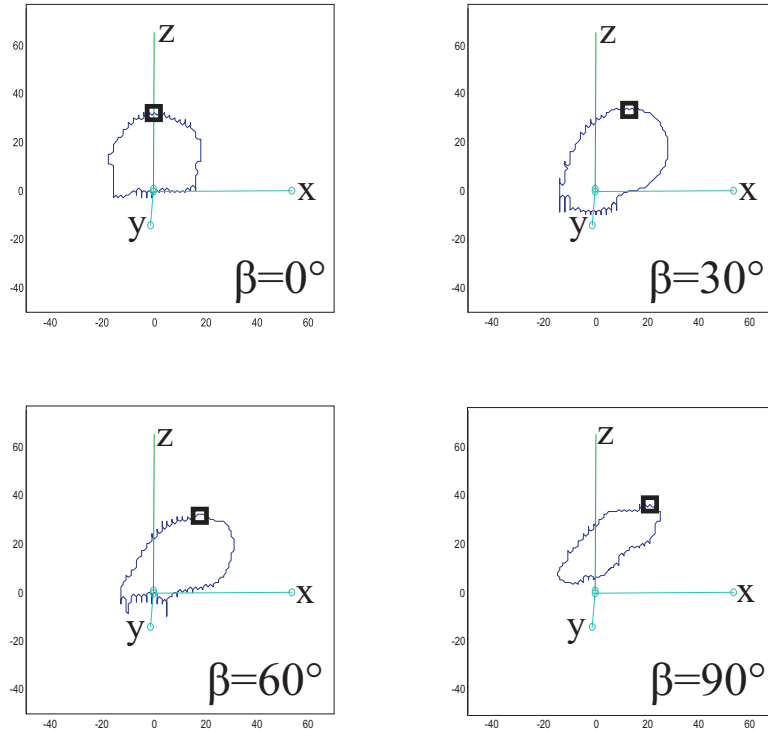
Figure 5.10: Melt pool borders in camera's image plane for different tangential directions. β represents the angle between the camera's line of sight φ and the clad's direction ψ. Bold square indicates top-most point on melt pool, used for height measurement.

5. With this shadow length, and knowing α (camera's angle with respect to the work plane), the height is calculated from Equation (5.9).
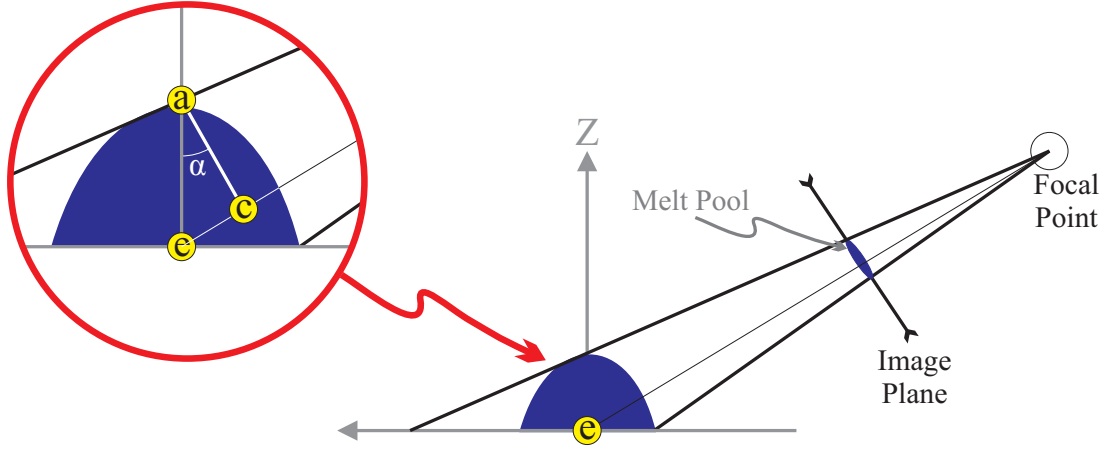
Figure 5.11: Schematic of third algorithm for extraction of clad height. This algorithm analyzes the image directly, without need to project coordinates into work plane.

5.2.4 Algorithm 3: Direct Height Estimate from Image

Before addressing the results, a third algorithm is developed. Looking at a cross-section of the clad, normal to the direction of motion ψ, one can derive a relationship between the clad's height, and the height of the melt pool in the image plane. Figure 5.11 illustrates the concept, whereby the height of the clad is estimated as

$$
\begin{aligned}
h &= |\overline{ae}| \\
&= |\overline{ac}| \csc(\alpha) \\
&= RL \csc(\alpha)
\end{aligned}
\tag{5.10}
$$

where $L\,[pixels]$ is the height of the clad, as measured in the image plane, $R\,[mm/pixel]$ is the magnification of the camera, and α is the camera's angle with respect to the substrate. The clad's height is measured in the image plane, in the direction of the z-axis, where the tangential direction ψ is taken as the substrate. It should be noted that $\angle ace$ is taken as 90°.

This new algorithm is independent of the clad's cross-section, along with the maximal height offset along the tangential direction, δ_o.

Table 5.1: Series of experiments to validate theoretical development of height equation (Equation (5.9)).

Experiment No.	β [*deg*]	Velocity [*mm/s*]	Experiment No.	β [*deg*]	Velocity [*mm/s*]
$1a$	0	0.75	$3a$	60	0.75
$1b$	0	1.25	$3b$	60	1.25
$1c$	0	1.75	$3c$	60	1.75
$1d$	0	2.25	$3d$	60	2.25
$1e$	0	2.75	$3e$	60	2.75
$2a$	30	0.75	$4a$	90	0.75
$2b$	30	1.25	$4b$	90	1.25
$2c$	30	1.75	$4c$	90	1.75
$2d$	30	2.25	$4d$	90	2.25
$2e$	30	2.75	$4e$	90	2.75

5.3 Experiments

To validate the theoretical developments resulting in Equation (5.9), several experiments were conducted at various angles between the tangential direction ψ and the camera's line of sight (i.e. varying β). Also, various velocities were selected, resulting in different clad heights. The experiments are listed in Table 5.1.

The experiments were conducted with a pulse frequency of $90\,Hz$, $4\,J/pulse$, and a $3\,msec$ pulse duration, corresponding to approximately $360\,W$ of energy. 304L stainless steel was delivered to the melt pool at a rate of $2\,g/min$. The interaction zone was monitored by one Sony SM183 analog camera, whose optical system comprised a bandpass filtered centered at $700\,nm$ and neutral density filter (*e.g.* welding shield) of number 8. Images were captured at a rate of $10\,Hz$ through a National Instruments LabView Real-Time system, where the height algorithm was applied offline. In addition to capturing images, the LabView system controlled a 3-axis motion system for producing the desired trajectories. The true height of the deposited clads were obtained through a digital microscope, capable of recording magnified images. These images were subsequently passed to a simple image processing algorithm, based on the magnification scale, to measure the height of clads. The accuracy was found to be $\sim 13\mu m$.

5.4 Results and Discussion

In the theoretical development of Section 5.2, three height algorithms were discussed. The first algorithm was set aside due to its sensitivity to melt pool shape, a problematic issue for real data. The second algorithm was given an in-depth analysis, upon which practical physical phenomena could be related with. The third algorithm was a quick glance at another possible technique for height extraction, however, was taken more as a future recommendation. For these reasons, only algorithm 2 will be applied to the experiments listed in Table 5.1.

Figure 5.12(a) illustrates both the true and estimated clad heights, with black and gray curves respectively. The height estimate is obtained from algorithm 2, however, without including the effect of height offset δ_o along the clad's direction of motion ψ. Two things should be noticed from these results: 1) the estimates follow the proper dynamics of the true clads and, 2) there is a large bias for all estimates of all experiments.

First, Figure 5.12(b) illustrates a closer look at the results of experiment 4b, illustrating that algorithm 2 does provide a good estimate to the true height as the dynamics are properly captured. This demonstrates that the location at which the shadow is measured properly relates to the actual clad height. That is, as the clad grows or shrinks, both the time and magnitude are captured by the algorithm. However, the bias explains that the length of the shadow, or the origin from which it is taken, is not correct.

For verification of algorithm 2's functionality, it was applied to the estimation of a $2mm$-cube, with errors less than $0.07mm$ (see Figure 5.6 for more details). The only difference from this experiment to those of Table 5.1 is the addition of a neutral density shield to the optical system. After a quick investigation, it is concluded that this piece of glass causes refraction of incoming light, thus translating the melt pool. Since the length of shadows are measured from the melt pool's boundary back to the laser's center-point, the shadow lengths become longer, and thus, larger height estimates incur. This was corrected by shifting the laser center-point by an amount equal to that observed during refraction. Figure 5.13(a) illustrates images with and without welding shields. A point is identified in both images, which gets translated
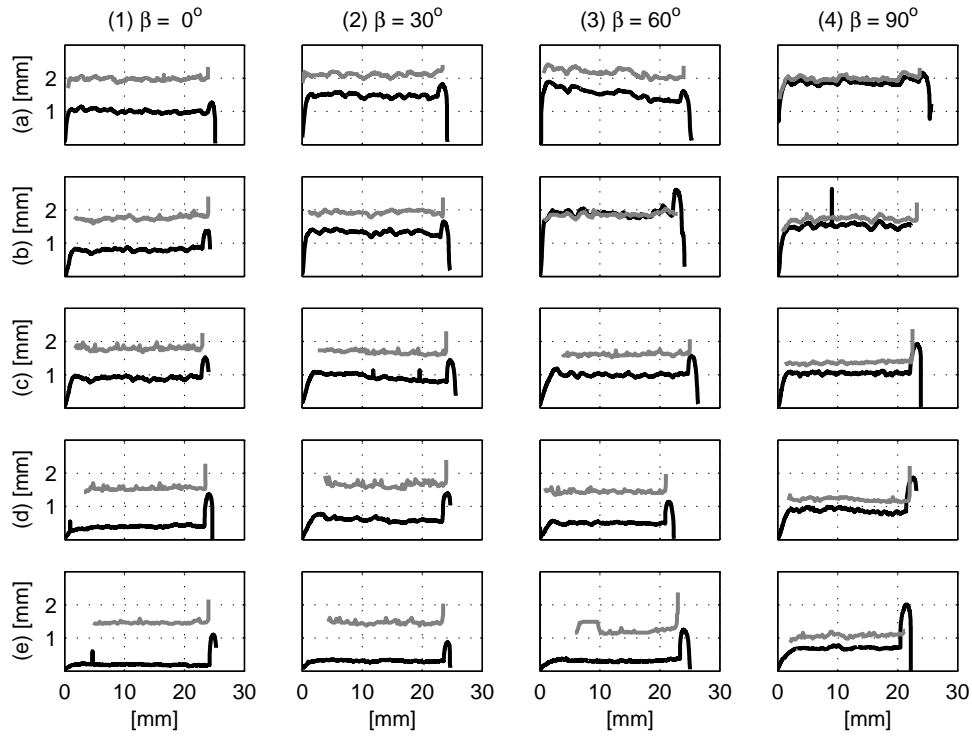
(a) Comparison of height estimate and true height for all experiments listed in Table 5.1. Black: true height, gray: algorithm 2 estimate.
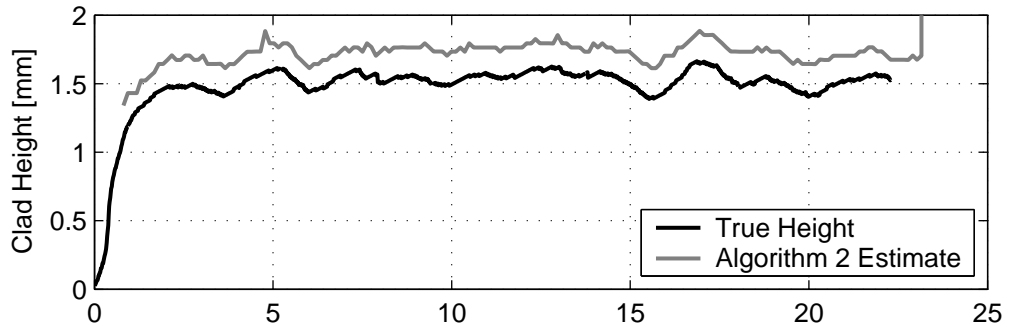
(b) Result of experiment 4b, illustrating that dynamics are properly estimated using algorithm 2.

Figure 5.12: Results of applying height algorithm 2 for experiments listed in Table 5.1. Height estimates do not include height offset δ_o along direction of motion ψ.

by (14,8) pixels (see Appendix B for further details on refraction). As a result of shifting the laser's centre-point by this latter amount, the corrected height estimates have an improved accuracy, as shown in Figure 5.13(b). The estimates are better however, still contain some bias.

This remaining bias can partially be explained by the introduction of height offset δ into the estimation, as outlined in the development of algorithm 2. As previously mentioned, the offset is dependent upon two things: the substrate's velocity v, and the angle between camera and clad direction, β. The relationship between velocity and offset was shown in Figure 5.9 as $\delta_o = (0.94 - 0.39v + 0.05v^2)$, while the effect of β is given by the cosine of this angle. The author proposes incorporating these two effects into the final height as follows:

$$h = \left[S - \overbrace{\left(0.94 - 0.39v + 0.05v^2\right)\cos\left(\beta\right)}^{\text{Height Offset } \delta_o \text{ Along } \psi} \right] \tan\left(\alpha\right) \qquad (5.11)$$
$$\underbrace{\hphantom{S - \left(0.94 - 0.39v + 0.05v^2\right)\cos\left(\beta\right)}}_{\text{Adjusted Shadow Length}}$$

The results of this adjustment are found in Figure 5.14. The new findings have slightly increased the accuracy of the estimates, however, it appears the values obtained in Figure 5.9 are not very suitable (*i.e.* the offset's relationship to substrate velocity). This can largely be attributed to the dependence of clad formation on its direction of motion, relative to that of the powder nozzle. That is, the nozzle utilized in this setup has a lateral configuration, and therefore, has a preferential direction ψ for optimal clad formation. This can be seen when comparing clad formations for constant velocities, however, varying the tangential direction ψ. For example, the first row of Figure 5.14 corresponds to depositions at a constant velocity of $v = 0.75mm/s$. A clad formation of nearly $2mm$ is achieved for $\beta = 90^o$, while only $1mm$ at $\beta = 0^o$. Larger clads require larger melt pools, which in turn have larger offsets δ_o at which the actual height is found. Thus, since the experimental setup is not capable of producing similar clad heights for varying tangential directions, the offset δ_o should be a function of height, as opposed to substrate velocity.

An additional attempt at understanding the problem of estimate bias was done through empirical measures. That is, each height estimate was manually offset by
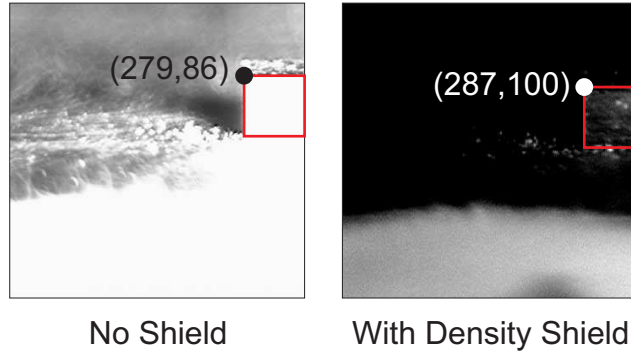
(a) Image taken of $2mm$-cube, with and without neutral density shield #8. Due to refraction, the image shifts by (14,8) pixels.
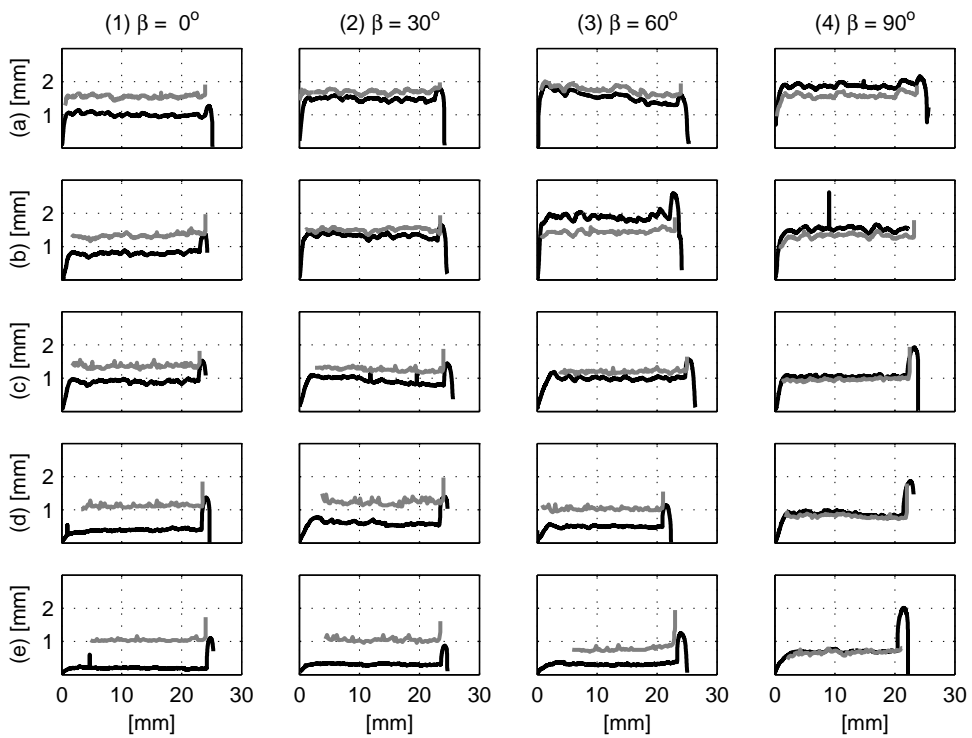
(b) Adjusted height estimates due to refraction.

Figure 5.13: Results of applying height algorithm 2 for experiments listed in Table 5.1. Estimates have been adjusted due to unexpected refraction through the optical system.
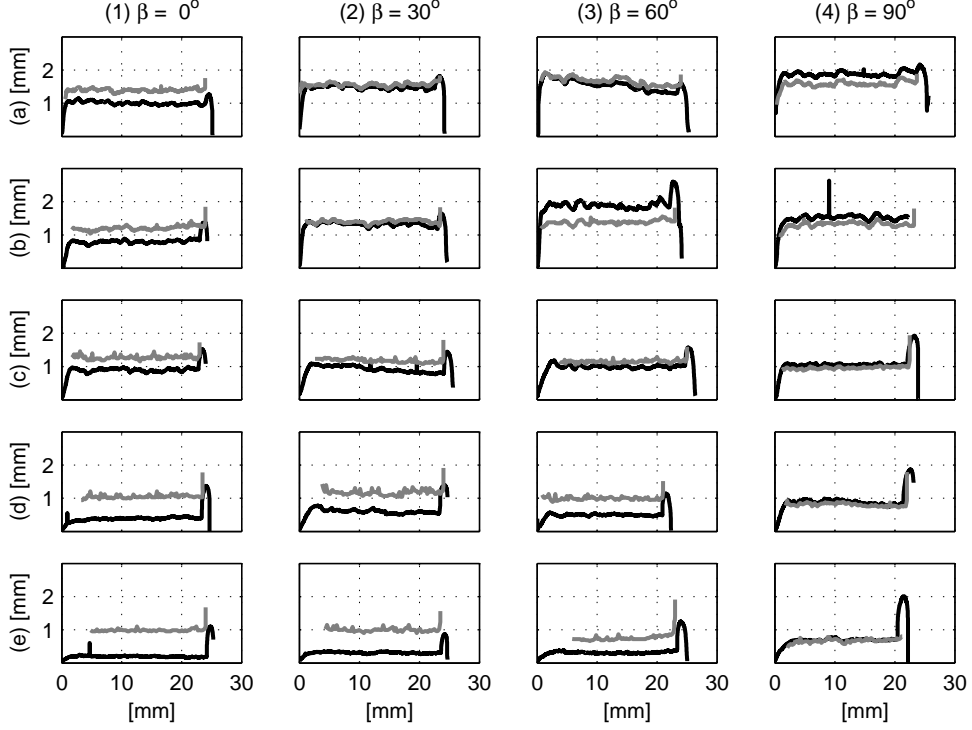
Figure 5.14: Height estimate using algorithm 2, with the inclusion of height offset δ_o along the clad's direction of motion ψ. The final offset removed from the shadow's length is: $\left(0.94 - 0.39v + 0.05v^2\right)\cos\left(\beta\right)$.

a given amount, namely dh. For example, looking at the results of experiment 1a of Figure 5.13(b), dh was set to $-0.5mm$. With this information gathered for all 20 experiments, it was now possible to relate the shift in height estimate back to the height's offset δ_o along ψ, such that:

$$\delta_o = -\frac{dh}{\cos\left(\beta\right)\tan\left(\alpha\right)}. \tag{5.12}$$

A plot of these results is found in Figure 5.15, for angles of 0° through 60° versus their respective velocities. Since the offset δ_o does not come into play for an angle of $\beta = 90^o$, it was not included. Also, it should be noted that experiments 3b and 3d produced abnormal results, and were omitted from this graph. There are two main features to notice from this graph: 1) the relationship between offset and velocity,
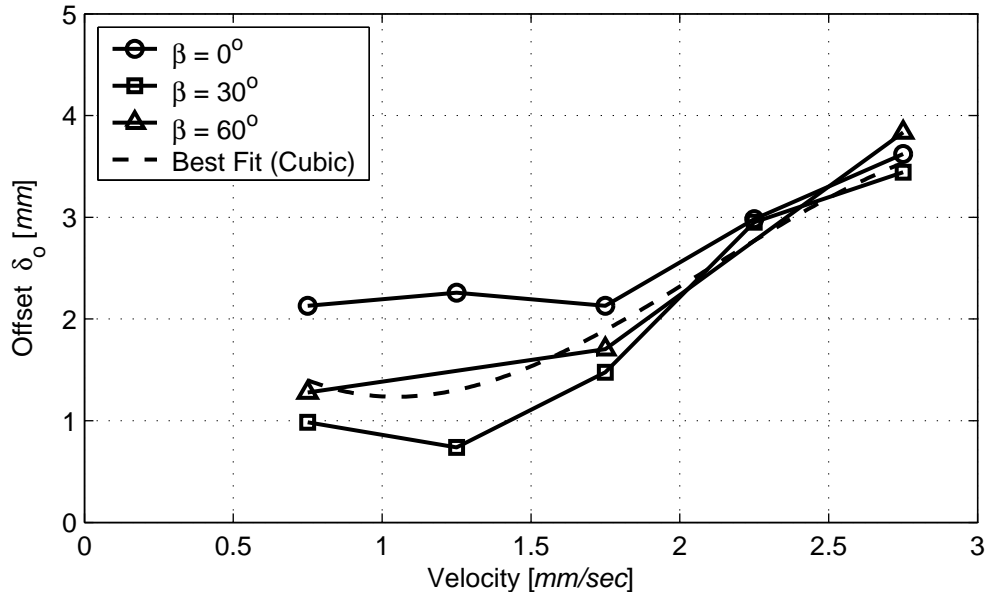
Figure 5.15: Calculation of bias required to obtain the nearest estimate possible to true clad height. Each test was adjusted by a specific amount, as shown in the graph. Tests 4 were not included, as the offset does not come into play, while tests 3b and 3d provided abnormal results and were equally omitted.

and 2) the magnitudes of height offsets.

First, as the velocity increases, the offset also increases, which is not anticipated. One possible reason for this unexpected trend is camera focus. When the optical system is setup, all adjustments are made with no density shield. When this shield is placed on the camera's lens, it is virtually impossible to see through the latter under normal lighting conditions. This makes it very difficult to properly align the camera, and set its focus. However, this last fact may be causing the problem. The camera's lens is focused at the laser center-point, without density shield. As this is added to the hardware, the camera's focus changes, as noticed when placing a shield of lesser density. Therefore, images are definitely out-of-focus, by an unknown amount. Now, this out-of-focus adds a hazy region around the melt pool, for example, of 10 pixels in width. Assuming two melt pools of largely different sizes, say 20 and 70 pixels in height (corresponding to approximately 0.5 and $2mm$, respectively). The addition of 10 pixels due to an out-of-focus camera has a much larger effect on the small clad ($\sim 50\%$) than with a larger clad ($\sim 14\%$). This may be the cause of height offsets

becoming larger for smaller clads. The rationale is that a smaller clad will have a smaller height offset, however, if there is an additional constant hazy region around this pool, the error is much larger, hence corrupting the trends, as seen here.

Second, the magnitudes of the offsets are much larger than previously observed. In Figure 5.9, the maximum offset has a magnitude of approximately $0.67mm$. However, in the latest trends of Figure 5.15, the maximum offset is roughly $3.85mm$. In general, offsets are many times greater than those previously observed. Remembering that the height offset δ_o essentially represents the length of the melt pool along its direction of travel ψ, it is difficult to understand how offsets of several millimeters can exist. This may be an indication that melt pools observed with the Sony SM183 analog camera may not be correct.

As a quick verification of these findings, a cubic function was fit to the height offset data of this latter figure. The resulting curve is now used in algorithm 2's height estimate, as shown in Figure 5.16. As seen, the estimates are much better, as expected since the bias has essentially been eliminated afterward. It would be very interesting to see if one is capable of reproducing these results.

The overall errors associated with each version of algorithm 2 are shown in Figure 5.17. As expected, the greatest errors occur for the original estimates, with no compensation for refraction through the density shield (triangle-series). As the refraction is accounted for (square-series), and with the introduction of height offset δ (pentagon-series), the errors reduce. By increasing the magnitudes of δ_o and reversing the expected trend of δ_o-versus-v, the errors are drastically reduced (circle-series). Table 5.4 summarizes these errors at each step.

As seen in both the figure and table, the maximum errors occur as the angle β is reduced. This is expected as the height offset is largest at $\beta = 0^o$. At the other extreme, the height offset does not influence the estimates for $\beta = 90^o$, and therefore, estimates should be very good at this angle. The fact that δ does not influence estimates at $\beta = 90^o$ should be utilized to ensure that the remainder of the algorithm is correct. Looking at the largest error in this series of experiments, namely 1a, the average error is 15%, or $0.30mm$. This would initially seem to be a good estimate, however, when looking at the standard deviation of this error, $0.04mm$, one can see that this is not random error, but rather, biased error. Thus, for simplest case of

Table 5.2: Estimate error in percentage of true height. Referring back to Figure 5.16, **Original** = red series, **With Refraction** = green series, **With Refr. & offset** δ_o **1** = blue series, and **With Refr. & offset** δ_o **2** = black series.

		Original	With Refraction	With Refr. & offset δ_o 1	With Refr. & offset δ_o 2
Test 1	a	-95	-53	-38	-21
	b	-116	-64	-49	-26
	c	100	-52	-42	-3
	d	292	-185	-166	-20
	e	-633	-422	-393	-5
Test 2	a	-49	-19	-9	1
	b	-45	-14	-6	6
	c	-83	-38	-28	4
	d	-179	-108	-97	-13
	e	-369	-236	-220	-6
Test 3	a	-40	-13	-8	-2
	b	1	23	26	31
	c	-63	-21	-16	1
	d	-197	-112	-104	-46
	e	-306	-150	-140	-15
Test 4	a	-6	15	15	15
	b	-13	14	14	14
	c	-30	9	9	9
	d	-38	8	8	8
	e	-53	4	4	4
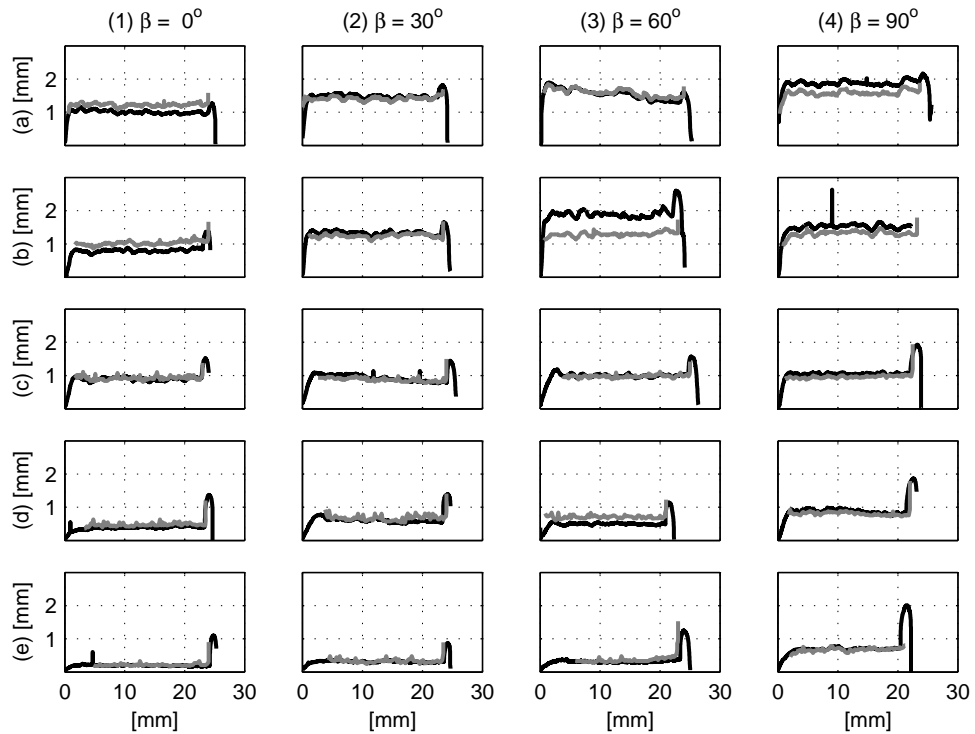
Figure 5.16: Height estimation using algorithm 2. These estimations have been optimized such that an attempt has been made to eliminate the bias. This was done by manually calculating the bias after estimation, and recalculating the function $\delta_o = f(v)$.

$\beta = 90^o$, there still exists bias in the estimate. This further solidifies the thought that melt pool images are not properly being captured.
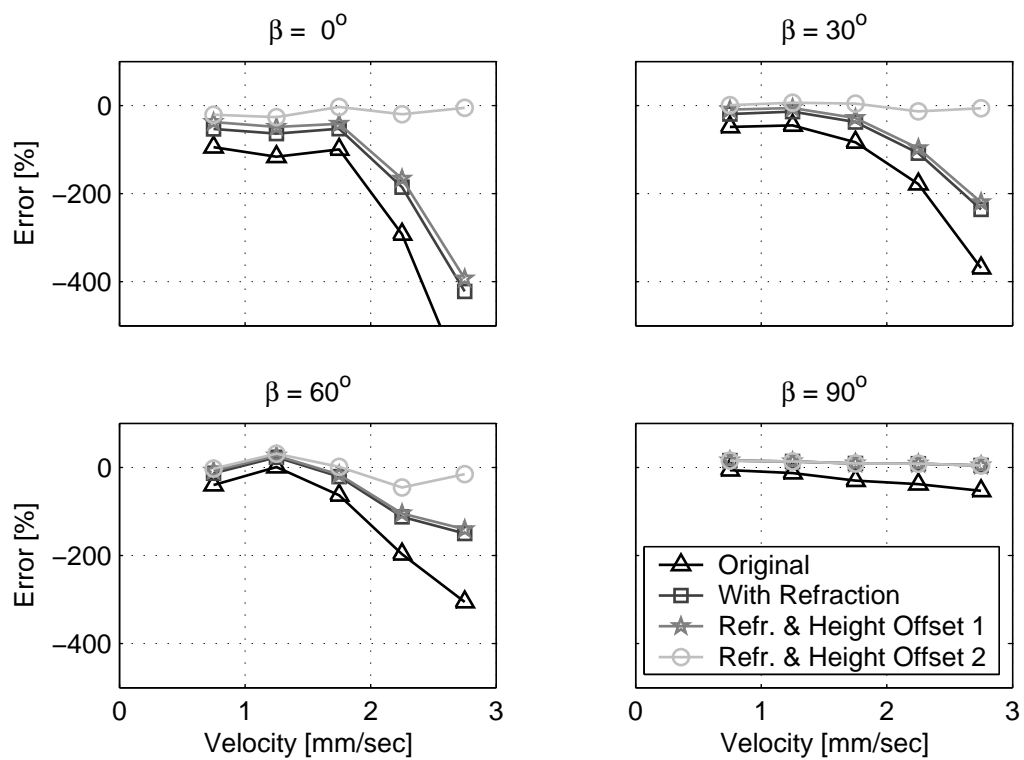
Figure 5.17: Percent errors associated with algorithm 2's estimation of true clad height. The different series correspond to the various modifications to the algorithm. See text for further explanation on each series.

5.5 Conclusions

In this chapter, melt pool boundaries were analyzed to extract height measurements of deposited clads. Three techniques were developed: intersection of two projections, shadow length of one projection, and direct height estimate from one image. In the first two algorithms, the perspective transformation was utilized to convert melt pool coordinates from the image plane to a work plane, coincident with the substrate upon which it was being deposited.

The first algorithm consisted of capturing two independent images of a melt pool, and projecting them onto the work plane. Due to the physical setup of the cameras, the front edge was common amongst the two images, and could therefore be used to extract the clad's width. From this width, an assumed elliptical cross-section for the clad allowed one to analytically determine the latter's height. The problem with this technique was the reliance upon the melt pool having a perfect shape near the substrate's intersection. This was not always the case, as the cross-section often varied, creating a false estimate of the clad's width, and therefore height. In theory, this algorithm should work, however, it was not practical.

In the second algorithm, the perspective projection of one camera was found to represent the melt pool's shadow, casted on the substrate. Knowing the angle of the camera, it was therefore possible to measure the length of the shadow, and using a right-angle triangle, calculate the height of the melt pool. The algorithm was tested with the picture of a $2mm$-cube, where it was revealed that measurement of shadow lengths were crucial. This lead to the inclusion of a height offset parameter, δ, which was the result of a constant height offset δ_o along the clad's tangential direction of motion ψ.

The last technique involved a quick analysis of the melt pool within the image itself. With the camera's resolution calculated, it was possible to measure the height of the clad, back to a line representative of its tangential direction of motion. This technique was not investigated for situations other than $\beta = 90^o$, and could be investigated in the future.

The second algorithm provided the simplest, yet most realistic model of height calculation, and was therefore applied to a set of 20 experiments. These were divided

into four groups, whereby a constant angle between camera and tangential direction of motion was established (from $\beta = 0^o$ to 90°). Within each group, five experiments were conducted, each at varying substrate velocities (0.75-$2.75\,mm/s$), which provided clads of differing heights.

The results revealed two important factors: first, refraction occurs through a neutral density shield, added to the optical system to reduce the light intensity seen by the analog camera, and second, the height offset δ is not properly modeled. The addition of a neutral density shield caused refraction of the incoming melt pool's light, shifting the laser's center-point, causing large errors. After this correction, it was noticed that the dynamics of the algorithm were very good, whereby clad growing-shrinking was very well estimated by the algorithm, however, with a constant bias. This bias was a function of both substrate velocity v and relative direction of motion β. Adjusting for height offset by introducing $\delta = (0.94 - 0.39v + 0.05v^2)\cos(\beta)$ reduced the bias, however, not sufficiently. By analyzing the bias for each experiment, an opposite trend was noticed: as substrate velocities increase, so does the height offset. This was the opposite of a trend previously observed by measuring clad offsets from a camera perpendicular to clad motion. This should therefore be further investigated, as the measurement of the clad's shadow is crucial to removing this bias.

Table 5.4 provides a list of experimental errors for all tests, and all modifications to the algorithm. The last two columns represent the best errors obtained. In the last column, the bias was calculated after the experiments were finished, and then removed, which is why the errors are very low. The third column has the most realistic errors, whereby results are best for $\beta = 90^o$ (4-15%), and worst for $\beta = 0^o$ (38-393%). The algorithm should therefore be tested for angles near $\beta = 90^o$ since the clad's offset has little to no effect on the results. With this condition properly accounted for, one can investigate the effect of δ for angles nearing $\beta = 0^o$.

In addition, for all angles of β, the algorithm appears to work best at low velocities, which correspond to large clad formations. Large clad formations result in large melt pools in the captured images, which may lead to certain hypotheses as to why the algorithm has such a large bias. For instance, if the image is not in focus, this will result in a melt pool slightly larger in circumference. With smaller melt pools, this represents a much larger percentage of its area, as opposed to large melt pools.

Thus, the error is also larger for smaller melt pools. In either case, this may provide a working range for the algorithm (v=0.75–1.75mm/s), or valuable insight as to improvements for the algorithm, such that it can perform well at higher velocities.

Chapter 6

Conclusions and Recommendations

6.1 Conclusions

In this thesis, analog cameras were used to extract height measurements of deposited clads in the laser cladding process. The steps involved in such a procedure can be categorized into three components: light analysis, melt pool segmentation, and feature extraction.

In Chapter 3, light irradiated from the process zone was analyzed, where it was determined to be dominated by blackbody radiation. From Planck's equation for blackbody radiation, and the non-linear attenuation of the CCD-sensor, theoretical trends of light, as observed from captured images of the process, were established (Figure 3.3). Experiments were conducted such that light from specific wavelengths was observed by a UNIQ 600CL digital camera. The captured images were analyzed by calculating optimal threshold levels, a measure of light intensity from an image. As predicted, the captured light followed the bell-shaped trends, peaking at approximately $700nm$. For this reason, and due to stable light conditions, narrow bandpass filters centered at this latter wavelength were added to the camera's optical hardware.

In Chapter 4, images were taken through a pair a image processing techniques, whereby the final output was a series of coordinates, in the image plane, of the melt pool's border. First, a grayscale image was thresholded by use of binarization techniques. The main goal of binarization was to properly associate pixels to either the background, or the melt pool. The main difficulties arose due to a hazy region around

the latter's border. Two techniques were investigated: Otsu and fuzzy entropy. Otsu's method largely concentrated on threshold levels near 50%, resulting in inclusion of this unwanted hazy region. On the other hand, minimization of fuzzy entropy produced threshold levels near 75%, which was able to properly segment the melt pool, with very little hazy region. After the image has been binarized, it remains to extract coordinates of the melt pool's border. For this, two categories of techniques were investigated: derivate- and comparison-based. Derivate strategies required a larger number of computations as spatial gradients were found at each pixel location. Also, border pixels did not arise in sequential order, but in a raster-manner. On the other hand, binarization was not required for this technique. Comparison-based methods performed very little computation at each pixel location (only comparisons of pixel values), and output pixel coordinates in a logical order, as the border is being traced in a clockwise fashion. For this reason, it was selected as the optimal technique to extract pixel coordinates.

In Chapter 5, the extracted melt pool coordinates were transformed into real-world coordinates, by use of a perspective transformation. This transformation produced the melt pool's shadow on the plane upon which it was being deposited. With the source of this shadow known (*i.e.* the camera), and measuring the length of the shadow, back to the location of clad height, it is possible to estimate the height of the object. This was confirmed through measurement of a $2mm$-cube, with very good accuracy ($< 3.5\%$ error). Applying the algorithm to melt pool images revealed the need to further investigate the location at which clad height is measured. Due to the symmetry of a $2mm$-cube, it is rather easy to determine the location of height. For melt pools, an extra parameter, δ, was subtracted from the shadow's measurement to incorporate the effect of clad height being offset from the laser's center-point. A relationship was developed such that δ decreased with both velocity v and the angle between camera and clad's direction of motion, β. 20 experiments were conducted, varying both v and β. The results revealed very good dynamics, whereby excellent approximation of the shrinking-growing of the clad was accomplished. However, a large bias existed, varying with both parameters. Analyzing this bias revealed an opposite trend for δ. That is, δ decreased with increasing β, as expected, however, increased with faster velocities, which was not expected. This last comment required could be

attributed to the camera being out-of-focus, but should be further investigated to see if the trends can be reproduced.

Experimental errors were found to be lowest for $\beta = 90^o$, ranging from 4 to 15% error. On the other hand, as β decreased to zero, so did the accuracy of the estimates. Largest errors were found at $\beta = 0^o$, ranging from 38 to 393%. The errors were almost completely attributed to the bias in the estimates, as standard deviations were extremely small.

Although the algorithm should work for all angles β, these preliminary findings illustrate that better results will be obtained for angles approaching 90°. Thus, keeping the camera as perpendicular as possible to the deposition track will, in the case of these results, provide the best estimate of the solidified height. Also, a working range for the substrate's velocity is in order, such that keeping these lower than $1.75mm/s$ provides the best estimates, for all angles of β. In addition, due to the use of an optical density shield causing refraction, it is required to perform identification of this translation for each experimental setup.

6.2   Recommendations

From the results of Chapter 5, the large problem with the algorithm is the amount of bias in the estimate. The bias appears to be related to the height offset δ_o along the direction of motion ψ. This is relatively clear since the algorithm is capable of working with the image of a $2mm$-cube, where the height offset is very clear. Thus, two conclusions arise regarding the origin of this bias: first, the images captured are possibly corrupt, and second, further investigation of verification of the height offset are required. The following recommendations are largely based on these two observations.

1. Images captured with the UNIQ 600CL digital camera had much better quality. First, the camera has a digital gain, which capable of reproducing the effects of the neutral density shield, without refraction. Also, this will eliminate the problem of images possibly being out-of-focus. Second, images have more information as saturation is less prominent. With the Sony SM183 analog

camera, the melt pool is essentially white, with very little hazy region, while the background is black. The images also have a "banding" effet, which is said to be a cause of CCD-saturation, as mentioned by the supplier in the provided document. On the other hand, the digital camera provides a better grayscale image, where previously solidified clads can be seen alongside the melt pool. This almost guarantees that the melt pool's size is properly captured. The only disadvantage to these digital cameras are the sudden "explosions" that occur. These abnormal phenomena should be further investigated, especially with help from the supplier.

2. The laser's center-point often appears just outside the melt pool. This should be further investigated by properly selecting trajectories of varying directions. That is, one trajectory of interest is to deposit a clad with $\beta = 90^o$, where the two line-up properly. Then, a sudden of $\beta = 0^o$ should provide good insight as to where the center-point is located, depending on the direction of travel. At this point, the phenomena is associated with refraction through the optical hardware, however, such tests can fully verify the hypothesis. This type of testing requires further programming of the NI LabView software as only simple, one point trajectories can be accomplished at this moment.

3. Further investigation of the height offset δ_o along the direction of travel ψ should be done, as this appears to be the main contribution to the bias. Placing a camera perpendicular to the direction of travel should provide a good view of the process, and with various parameters such as velocity and nozzle placement, should yield a better understanding of this parameter. Possibly investigating the relationship of this offset with respect to estimated height could also produce a good result.

4. Including two cameras into the algorithm will not increase this algorithm's accuracy. This is due to the fact that the same algorithm is applied but to a camera with a different view of the melt pool. As shown in the results, there is only a small range of camera angles which yield good results. Therefore, adding a second camera with a drastically different view of the melt pool will only provide worse estimates. On the other hand, addition of a second camera may

help for a different algorithm, which properly combines the information from each view into one estimate. However, from the results shown in this thesis, it appears one camera is sufficient since the majority of the error is attributed to a bias.

5. The nozzle placement is crucial for all types of experiments, and more attention should be placed on creating a proper fixture for fine tuning. Also, it should be adjusted for optimal catchment efficiency, such that it is virtually independent of deposition trajectories.

6. The algorithm lends itself well to application in real-time. Each sub-component is rather simple, where simple comparison-instructions are used to obtain the information. First, a look-up-table can be used to greatly reduce the speed at which fuzzy thresholds are obtained. On a QNX platform (Pentium 4, $2.8\,GHz$ single processor), speeds upwards of $100\,Hz$ were obtained. In addition, the border tracing algorithm requires even less time to operate as it merely uses comparisons at each pixel location. Next, conversion from image plane to world plane need only be done for the one pixel selected as the height's shadow point. Last, a few equations of simple multiplication and addition are performed to yield the height. Thus, the algorithm itself is very rapid. However, the limiting factor is the capture-rate of the cameras. With two UNIQ 600CL digital cameras on the same QNX platform, speeds approaching $40\,Hz$ where obtained, without saving images to memory. On the NI Real-Time platform, with comparable processor speed, the is drastically reduced to around 15-20Hz.

Bibliography

[1] M. Dickens, "Rapid prototypingthe ultimate in automation," *Assembly Automation*, vol. 14, no. 2, pp. 10–13, 1994.

[2] K. Watkins, "Achieving the potential of direct fabrication with lasers," *Proceedings of 3rd International Conference on Laser Assisted Net Shaping*, pp. 25–38, 2001.

[3] N. Waterman, "Rapid product development in the usa, europe and japan," *World Class Design to Manufacture*, vol. 1, no. 3, pp. 27–36, 1994.

[4] D. Pham and R. Gault, "A comparison of rapid prototyping technologies," *International Journal of Machine Tools and Manufacture*, vol. 38, no. 10-11, pp. 1257–1287, 1998.

[5] X. Yan and P. Gu, "A review of rapid prototyping technologies and systems," *Computer-Aided-Design*, vol. 28, pp. 307–318, 1996.

[6] N. Juster, "Rapid prototyping using the selective sintering process," *Assembly Automation*, vol. 14, no. 2, pp. 14–17, 1994.

[7] F. Klocke, T. Celiker, and Y.-A. Song, "Rapid metal tooling," *Rapid Prototyping Journal*, vol. 1, no. 3, pp. 32–42, 1995.

[8] E. Sachs and E. Vezzetti, "Numerical simulation of deposition process for a new 3dp printhead design," *Journal of Materials Processing Technology*, vol. 161, pp. 509–515, 2004.

[9] A. Huang, S. Nolan, and M. Brandt, "Pre-placed wc/ni clad layers produced with a pulsed nd:yag laser via optical fibres," *Surface and Coatings Technology*, vol. 165, pp. 26–34, 2003.

[10] F. Meriaudeau, F. Truchetet, C. Dumont, and P. Bolland, "Acquisition and image processingsystem able to optimize laser cladding process," *Proceedings of ICSP*, pp. 1628–1631, 1996.

[11] F. Meriaudeau and F. Truchetet, "Control and optimization of the laser cladding-process using matrix cameras and image processing," *Journal of Laser Applications*, vol. 8, pp. 317–324, 1996.

[12] F. Meriaudeau, F. Truchetet, D. Grevey, and A. Vannes, "Laser cladding process and imageprocessing," *Laser In Engineering*, vol. 6, pp. 161–187, 1997.

[13] M. Doubenskaia, P. Bertrand, and I. Smurov, "Optical monitoring of nd:yag laser cladding," *Thin Solid Films*, vol. 453-454, pp. 477–485, 2004.

[14] M. Ignatiev, I. Smurov, V. Senchenko, V. Dozhdikov, and P. Bertrand *International Thermal Spray Conference*, pp. 1001–1006, 2002.

[15] L. Li and W. Steen, "In-process clad quality monitoring using optical method," *Proceedings of SPIE: Laser-Assisted Processing II*, vol. 1279, pp. 89–100, 1990.

[16] M. Fox, D. Hand, D. Su, J. Jones, S. Morgan, M. McLean, and W. Steen, "Optical sensor to monitor and control temperature and build height ofthe laser direct-casting process," *Applied Optics*, vol. 37, pp. 8429–8433, 1998.

[17] F. Haran, D. Hand, C. Peters, and J. Jones, "Focus control system for laserwelding," *Applied Optics*, vol. 36, pp. 5246–5251, 1997.

[18] J. Mazumder, A. Schifferer, and J. Choi, "Direct materials deposition: designed macro andmicrostructure," *Material Research Innovations*, vol. 3, no. 3, pp. 118–131, 1999.

[19] L. Han, F. Liou, and K. Phatak, "Modeling of laser cladding with powder injection," *Metallurgical and Materials Transactions B-Process Metallurgy and Materials Processing Science*, vol. 35, pp. 1139–1150, 2004.

[20] *Fundamentals of Heat and Mass Transfer, Fifth Edition.* John Wiley & Sons, 2002.

[21] M. Sezgin and B. Sankur, "Survey over image thresholding techniques and quantitative performance evaluation," *Journal of Electronic Imaging*, vol. 13, pp. 146–165, 2004.

[22] N. Otsu, "Threshold selection method from gray-level histograms," *IEEE transactions on Systems, Man and Cybernetics*, vol. 9, pp. 62–66, 1979.

[23] L. Wuang and L. Wang, "Image thresholding by minimizing the measures of fuzziness," *Pattern Recognition*, vol. 28, pp. 41–51, 1994.

[24] E. R. Davies, *Machine Vision: Theory, Algorithms, Practicalities, 2nd Edition.* Academic Press, 1997.

[25] R. T. R.D. Boyle, *Computer Vision: A First Course.* Blackwell Scientific Publications, 1997.

[26] V. S. Nalwa, *A guided tour of computer vision.* Addison-Wesley Publishing Company, 1993.

[27] R. Hartley and A. Zisserman, *Multiple View Geometry in Computer Vision.* Cambridge Press, 2003.

[28] E. Toyserkani, A. Khajepour, and M. Sameni, "Development of trinocular optical ccd-based detectors for real-time measurement of clad geometry," *Proceeding of International Congress on the Applications of Lasers and Electro-Optics*, pp. 93–100, 2004.

Appendix A

Solution of the Perspective Transformation Matrix, H

A perspective transformation is defined as the homogeneous transformation of a two-dimensional point from plane 0 to plane 1. The transformation is accomplished through a homogeneous transformation matrix $\mathbf{H}$, such that

$$P_1 = \mathbf{H}P_0 \tag{A.1}$$

where,

$$P_0 = \begin{pmatrix} x \\ y \\ 1 \end{pmatrix}, P_1 = \begin{pmatrix} WX \\ WY \\ W \end{pmatrix}, \text{and } \mathbf{H} = \begin{pmatrix} a & b & c \\ d & e & f \\ g & h & 1 \end{pmatrix}.$$

The original point P_0 has coordinates (x, y), which are placed into homogeneous format, as shown. The homogeneous matrix $\mathbf{H}$ is defined up to scale, with eight unknown parameters. The final result is a homogeneous representation of the original point, in the second plane, namely P_1. This point is equally defined up to scale, which is given by W. Therefore, to obtain Cartesian coordinates of the latter, one must divide P_1 by its third element:

$$(X, Y) = \left(\frac{P_1(1)}{P_1(3)}, \frac{P_1(2)}{P_1(3)} \right) \tag{A.2}$$

It remains to solve for the transformation matrix $\mathbf{H}$, which is uniquely defined for a set of two planes[1]. First, Equation (A.1) is decomposed such that,

$$\begin{pmatrix} WX \\ WY \\ W \end{pmatrix} = \begin{pmatrix} ax + by + c \\ dx + ey + f \\ gx + hy + 1 \end{pmatrix}. \tag{A.3}$$

Combining this last result with Equation (A.2), one can express the components of the output P_1 as

$$\begin{pmatrix} X \\ Y \end{pmatrix} = \begin{pmatrix} \frac{ax+by+c}{gx+hy+1} \\ \frac{dx+ey+f}{gx+hy+1} \end{pmatrix}. \tag{A.4}$$

Decomposing this vector equation as two separate equations, such that all unknown parameters are in present, yields:

$$\begin{aligned} xa + yb + 1c + 0d + 0e + 0f - xXg - yXh &= X \\ 0a + 0b + 0c + xd + ye + 1f - xYg - yYh &= Y. \end{aligned} \tag{A.5}$$

This can now be placed into matrix form, such that all input values are in matrices U and Y, and the unknown parameters are in a column-vector A. This is expressed as:

$$\underbrace{\begin{bmatrix} x & y & 1 & 0 & 0 & 0 & -xX & -yX \\ 0 & 0 & 0 & x & y & 1 & -xY & -yY. \end{bmatrix}}_{U} \underbrace{\begin{bmatrix} a \\ b \\ c \\ d \\ e \\ f \\ g \\ h \end{bmatrix}}_{A} = \underbrace{\begin{bmatrix} X \\ Y \end{bmatrix}}_{Y}. \tag{A.6}$$

---

[1]The following derivation is taken from Hartley and Zisserman [27]

A least-squares optimization is used to solve for the unknown parameters, such that

$$A = \left(U'U\right)^{-1} U'Y, \tag{A.7}$$

and hence the solution for our homogeneous transformation matrix **H**.

Since **H** has eight unknown parameters, one must have a minimum of eight data points. However, as seen, each point-correspondence creates two linearly independent equations, as shown in Equation (A.6). Therefore, it is only required to have a minimum of four point-correspondences to yield an exact solution. It is recommended however to have more than four, such that a better approximation may be found of the desired region.

Applying this to the problem at hand, solving for the homogeneous transformation matrix for the purpose of projecting melt pool borders from the image plane (taken as plane 0) to the substrate, or work plane (taken as plane 1), is summarized in the following four steps:

1. Place a minimum of four points on the work plane. Record the coordinates of all points using a well-defined Cartesian coordinate system and origin (*i.e.* intersection of laser with substrate, where alignment of X and Y axes are parallel to the motion of the CNC table beneath). These points can be placed on the surface by 'zapping' a point with the laser.

2. Setup the camera in the desired location, ensuring full view of all points. Take a picture of plane 1. Record the coordinates of the points as seen through in plane 0 (*i.e.* from the picture taken).

3. Match the points from the work plane to the image plane (point correspondence). For each point correspondence, construct the associated U and Y matrices of Equation (A.6). Each new point correspondence increases the number of row-vectors in the matrices (by a factor of 2).

4. Solve for the unknown parameters (A-matrix) with Equation (A.7).

Appendix B

Refraction of Melt Pool Irradiation

Refraction occurs when light travels from one medium to another. In the case of laser cladding, light irradiates from the melt pool and travels through the atmosphere. It then comes in contact with the welding shield, which is made of glass. The refraction can be measured through Snell's law, which states that:

$$n_1 \sin \theta_1 = n_2 \sin \theta_2, \tag{B.1}$$

where n is the index of refraction for mediums 1 and 2, and θ represents the angle with respect to the surface's normal, where subscripts 1 and 2 represent the incident and refracted light rays, respectively. Thus, if an incident ray is perpendicular to the surface (or in this case, the welding shield), then no refraction occurs.

The series of experiments listed in Table 5.1 were subjected to a translation due to refraction of the incoming light. At first, it was thought that the welding shield was not properly connected to the optical hardware, and thus light rays would hit the surface at an angle other than 90°, causing refraction. However, additional experiments were conducted whereby clear glass and this welding shield were further investigated. With the clear glass perpendicular to the camera's lens, no refraction could be observed. However, when replaced with the welding shield, refraction was observed as shown in Figure 5.13(a). One possible explanation lies in light rays being emitted at all angles. When these rays travel toward the camera, a small angle occurs, causing refraction. If the index of refraction n_2 is large enough, a substantial
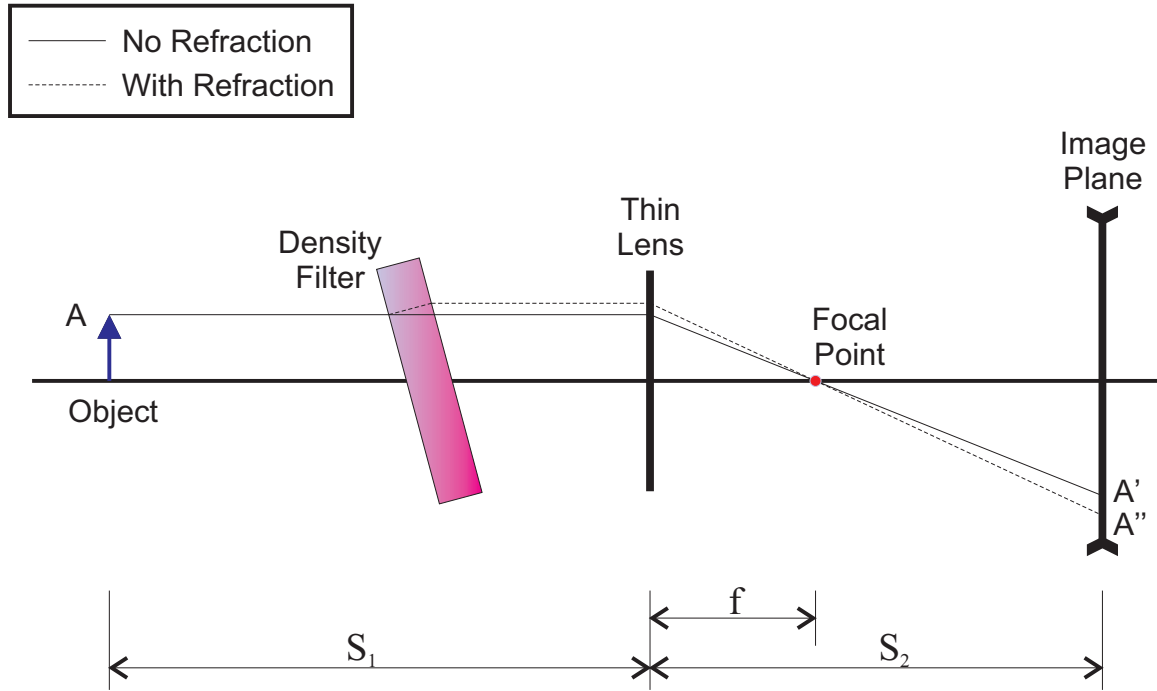
Figure B.1: Trajectory of light irradiating from melt pool.

refraction could occur. However, for common types of glass, the index of refraction is near 1.50, and as will be shown shortly, causes little deviation of the incoming ray.

Figure B.1 illustrates the basic trajectory taken by a light ray, with and without refraction through a different medium. As seen, refraction causes the point A' to shift, yielding A''. Equations of thin lenses are:

$$\frac{1}{S_1} + \frac{1}{S_2} = \frac{1}{f}, \text{ and } \frac{A}{A'} = \frac{S_1}{S_2},$$

where S_1, A and A' can be measured, leading to:

$$S_2 = S_1 \frac{A'}{A}, \text{ and } f = \left(\frac{1}{S_1} + \frac{A}{A'S_1}\right)^{-1}.$$

From snell's law, and assuming the density filter has thickness t, the deviation of

incoming rays to the thin lens is given as

$$\delta = t \left(\frac{\sin{(\theta_1 - \theta_2)}}{\cos{(\theta_2)}} \right), \tag{B.2}$$

where the refracted angle is:

$$\theta_2 = \sin^{-1} \left(\frac{n_1 \sin{\theta_1}}{n_2} \right).$$

Finally, using similar triangles between the thin lens and image plane, the final shift observed between A' and A'' is given as:

$$A'' - A' = \delta \left(\frac{S_2 - f}{f} \right) \tag{B.3}$$

From this equation, assuming common indices of refraction for air ($n_1 = 1.00$) and glass ($n_2 = 1.50$), incoming rays should be have $\theta_1 = 15^o$ to the welding shield's normal. This would cause a shift of approximately 14 pixels, as observed in the experiments. This is a rather large angle of incidence in regards to the overall magnitudes. The camera is approximately $500mm$ from the melt pool, which only has dimensions of $\sim 2mm$. The camera's field of view is roughly $10 \times 10 \ [mm]$, and therefore, irradiation from the melt pool should arrive at the camera nearly parallel to the its surface, with very little angle.

Appendix C

True Height Measurement of Clad

To evaluate the accuracy of the height algorithm it is necessary to have a reference height. This reference corresponds to the true height of the solidified clad, which is obtained by placing the latter beneath a microscope, where digital pictures are taken. Because the microscope magnifies the clad, multiple pictures must be taken of the overall length. Thus, each section of the clad is individually analyzed. Figure C.1 illustrates three samples images taken of a magnified clad. When the substrate and clad are placed under the microscope, a bright light is placed beneath the two, shinning directly upward toward the camera. This produces a very binarized image, whereby the clad is very dark while the remainder of the image is light.

Each image is then thresholded, where a static threshold level is selected based
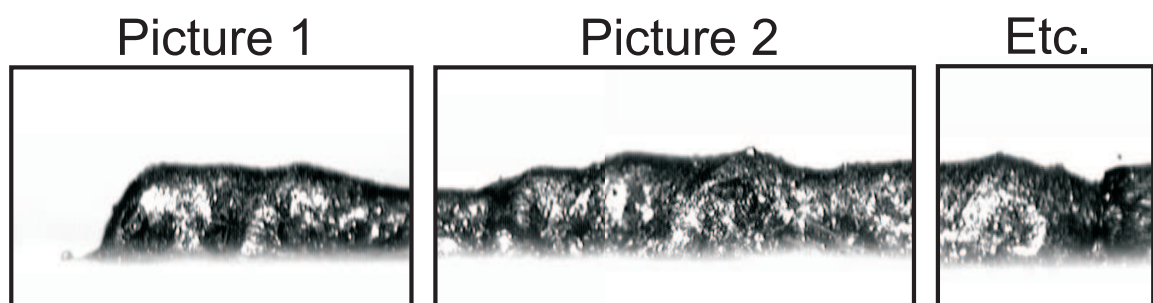
Figure C.1: Images captured from a microscope of a sample clad. Multiple images must exist due to the magnification and the length of the clad. A bright light is placed beneath the sample, thus enhancing the view of the clad.
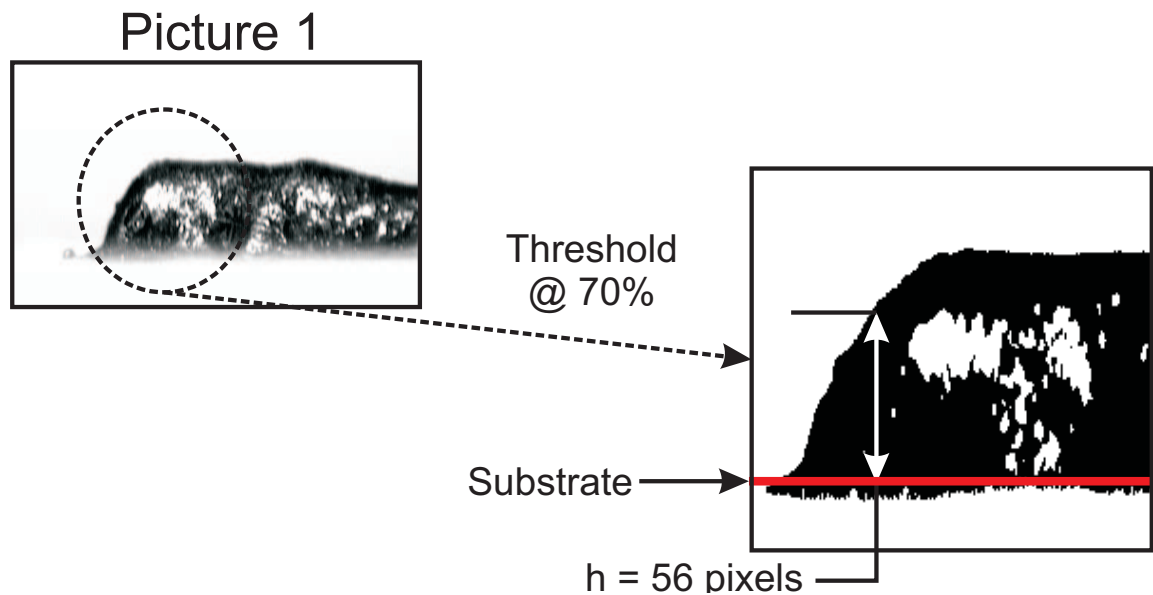
Figure C.2: A static threshold of 70% is used to binarize a portion of Picture 1. The substrate is then located, shown here with a thick red line. The height at each column in the image is then measured, in terms of pixels.

upon expert knowledge. The substrate is located, where a reference line is drawn on the image. The clad's height is then obtained by counting the number of pixels from substrate to the clad's top surface. This is done for each column in the picture. Figure C.2 illustrates the concept for Picture 1.

To convert heights from pixels to millimeters, a reference object is placed under the microscope, where an image is captured with the same magnification used for the clad pictures. From this image, the magnification can be obtained from the ratio of the reference object's height in millimeters, to the height in the image in units of pixels. For the sample image shown in the previous figures, the ratio corresponds to $13\mu m/pixel$, yielding a height of $0.728mm$ for that shown in Figure C.2.